FABRICATION AND CHARACTERIZATION OF GRAPHENE/SILICON BASED SCHOTTKY PHOTODIODE

A Thesis Submitted to
the Graduate School of Engineering and Sciences of
İzmir Institute of Technology
in Partial Fulfillment of the Requirements for the Degree of

MASTER OF SCIENCE

in Photonics Science and Engineering

by

Gülçin DÖNMEZ

December 2019

İZMİR

We approve the thesis of **Gülçin DÖNMEZ**

Examining Committee Members:

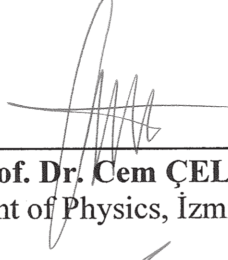

Assoc. Prof. Dr. Cem ÇELEBİ
Department of Physics, İzmir Institute of Technology

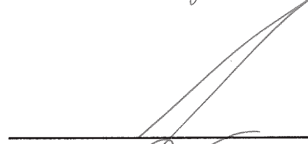

Assoc. Prof. Dr. Sinan BALCI
Department of Photonics, İzmir Institute of Technology

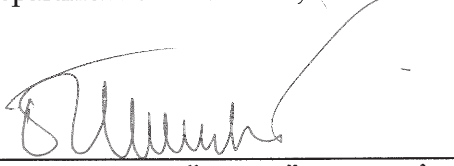

Asst. Prof. Dr. Özhan ÜNVERDİ
Department of Electrical and Electronics Engineering, Yaşar University

9 December 2019

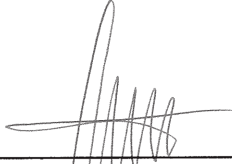

Assoc. Prof. Dr. Cem ÇELEBİ
Supervisor, Department of Physics,
İzmir Institute of Technology

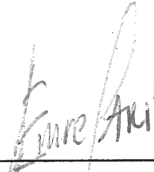

Asst. Prof. Dr. Emre SARI
Co-Supervisor, Department of Photonics,
İzmir Institute of Technology

Prof. Dr. Canan VARLIKLI
Head of the Department of Photonics

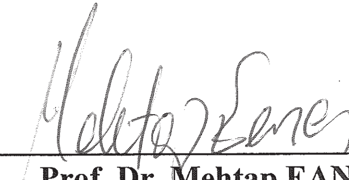

Prof. Dr. Mehtap EANES
Dean of the Graduate School of
Engineering and Sciences

ACKNOWLEDGMENTS

It is my pleasure to acknowledge and express my gratitude those who helped me along the way to completion of this thesis.

Firstly, I would like to thank my parents, sister and brother for all of their patience and support through the whole process of my study. They did everything for my future and happiness.

I would like to thank my advisor Assoc. Prof. Dr. Cem Çelebi for his patience, invaluable help, guidance, encouragement detailed reviewing all of my study. Without their support and guidance, I would never have been able to complete this study.

I wish to thank the other committee members of my thesis Assoc. Prof. Dr. Sinan Balcı and Assst. Prof. (PhD) Özhan Ünverdi for their participation and comments.

I would like to acknowledge my lab mates and friends; Alper Yanılmaz, Mehmet Fidan, Yasemin Keskin, Nusret Şahan, Sinem Duman, Fulya Koç and Elçin Şahin for their experimental knowledge and support during my study.

I also would like to thank Hatice İlhan, Sevgi Serkir, Aysu Yıldırım and Dilara Tarım for their valuable friendship and support.

ABSTRACT

FABRICATION AND CHARACTERIZATION OF GRAPHENE/SILICON BASED SCHOTTKY PHOTODIODE

This thesis focused on fabrication and characterization of CVD grown p-type graphene and n-type Si Schottky junction photodiode with rectification behavior. The device operated at wavelength range between 390 and 1100 nm at self-powered mode. The device was encapsulated with Epoxy Resin to prevent graphene from atmospheric adsorbates. The electronic and optoelectronic characterizations of the devices were done before and after coating the devices with ER. By encapsulation stability of the device was enhanced in terms of photoresponsivity. The maximum obtained photoresponsivity value of the bare device was 0.56 A/W. Also, time-resolved photocurrent spectroscopy measurements showed that the devices exhibited enhanced photodetector performance in terms of photo-switching characteristics.

Furthermore, electrical characteristics of Gr/n-Si Schottky photodiode under various illumination power densities with 850 nm wavelength were investigated. The short circuit current showed linear response to power density. However, open circuit voltage exhibited two phased slow and fast increment with increased power density. Hall effect measurements were conducted in order to investigate hole carrier concentration and mobility of the graphene on n-Si. With increasing the power density the carrier concentration increased and the mobility decreased. Besides, light induced manipulation of the Schottky barrier height of Gr/n-Si photodiode was studied. Schottky barrier height of the graphene measured by KPFM method as 0.4 eV. With increasing power density we found that Schottky barrier height of the device increased from 0.4 eV to 0.5 eV and showed similar trend with the change in open circuit voltage.

ÖZET

GRAFEN/SİLİKON TABANLI SCHOTTKY FOTODİYOTUN FABRİKASYON VE KARAKTERİZASYONU

Bu tez, Kimyasal Buhar Biriktirme yöntemi ile üretilen p-tipi grafen ve n-tipi Silikon (Gr/n-Si) Schottky eklem fotodiyotunun fabrikasyonu ve karakterizasyonuna odaklanmıştır. Grafen ve n-Si Schottky eklemi doğrultucu bir davranış göstermiştir. Elde edilen aygıt ile 390-1100 nm dalgaboyu aralığında ve fotovoltaik modda ölçümler alınmıştır. Ayrıca cihaz Epoksi reçine ile kaplanarak hava ile teması kesilmiş ve böylece aygıtın daha stabil hale getirilmesi amaçlanmıştır. Aygıt enkapsüle edilmeden önce ve sonra elektriksel ve optoelektriksel karakterizasyonu yapılmıştır.

Günlere bağlı yapılan fotocevap ölçümleri enkapsülasyon işleminin aygıtın stabilitesini arttırdığını göstermiştir. Elde edilen maksimum fotocevap değeri enkapsüle edilmemiş aygıt için 0.56 A/W olarak ölçülmüştür. Ayrıca zamana bağlı fotoakım spektrometresi ölçümleri aygıtların açma kapama performansları bakımından gelişmiş bir fotodetektör performansı sergilediğini göstermiştir.

Buna ek olarak, Gr/n-Si Schottky fotodiyotun 850 nm dalga boyunda farklı şiddetlere sahip ışık altında elektriksel karakteristiğindeki değişim incelenmiştir. Kısa devre akımı artan ışık şiddeti ile doğru orantılı artmıştır. Fakat açık devre voltajı artan ışık şiddetine bağlı olarak yavaş ve hızlı olmak üzere iki fazlı bir artış göstermiştir. Işık şiddetine bağlı olarak n-Si üzerindeki grafenin deşik yoğunluğu konsantrasyonunu ve mobilitesini ölçmek için Hall Etkisi ölçümleri yapılmıştır. Işık şiddetine bağlı olarak deşik konsantrasyonu artmış fakat mobilite düşmüştür. n-Si üzerindeki grafenin Schottky bariyer yüksekliği Kelvin Kuvvet Aygıtı Mikroskopu (KPFM) yöntemiyle 0.4 eV olarak ölçülmüştür. Ayrıca, Gr/n-Si fotodiyotun Schottky bariyer yüksekliğinin ışık şiddeti ile değişimi incelenmiştir. Artan ışık şiddetiyle birlikte, aygıtın Schottky bariyer yüksekliğinin 0.4 eV'den 0.5 eV'ye yükselmiştir ve bu değişim açık devre voltajındaki değişimle benzer bir eğilim göstermektedir.

To my dear family,

TABLE OF CONTENTS

LIST OF FIGURES ix

LIST OF TABLES xiii

LIST OF ABBREVIATIONS xiv

CHAPTER 1. INTRODUCTION 1
1.1. Graphene 2
1.2. Physics of Schottky Junction 7
1.3. Graphene/Semiconductor Heterojunction 10
1.4. p-type Graphene/n-Si Heterojunction 12

CHAPTER 2. EXPERIMENTAL 17
2.1. Growth of Graphene by CVD Method 17
2.2. Transfer of Graphene on to SiO_2/n-Si Substrate 19
2.3. Fabrication of Graphene/Silicon Schottky Devices 20
2.4. Characterization Techniques 20
2.4.1. Optical Microscopy 21
2.4.2. Raman Spectroscopy Measurement Technique 22
2.4.3. Kelvin Probe Force Microscopy 24
2.4.4. Electronic and Optoelectronic Measurements Setup 25
2.4.4.1. Photocurrent Spectroscopy Setup 26
2.4.4.2. Probe Station 27

CHAPTER 3. RESULTS AND DISCUSSION 30
3.1. Characterization of Gr/n-Si Schottky Diodes 30
3.1.1. Optical Microscope and Raman Spectroscopy Measurements 30
3.1.2. KPFM Analysis 31
3.1.3. Electrical Characterization of Gr/n-Si Schottky Diodes 32
3.2. Electronic and Optoelectronic Characterization of Gr/n-Si Photodiodes 34
3.2.1. Electronic Characterization of Gr/n-Si Photodiodes 34

3.2.2. Photoresponsivity of Gr/n-Si Photodiodes 38
3.3. Electrical characteristics of Gr/n-Si Schottky Photodiode under illumination with various power density 40

CHAPTER 4. CONCLUSION 44

REFERENCES 46

LIST OF FIGURES

Figure **Page**

Figure 1. Schematic illustration of sp^2 hybridization in graphene unit cell...................... 3

Figure 2. (a) Honeycomb lattice structure of graphene. The unit cell consists of two atoms labeled A and B, the lattice vectors are a_1 and a_2. (b) First Brillouin zone of graphene with reciprocal lattice vectors b_1 and $b_2$as a function of k_x and k_y and (c) Brillouin zone of graphene with representation of Dirac cones near the K and K'points.. 4

Figure 3. Linear dispersion (Dirac cone) representation with conduction and valence bands through the K point (Dirac point). With charge transfer to or from the graphene leads electron or hole doping which replaced the Fermi Level above or below to the Dirac point. 5

Figure 4. The optical transmittance of transparent conductive electrodes that are used commercially for UV, visible and NIR regimes. 6

Figure 5. Ideal Metal/n- type semiconductor band diagram (a) Seperate and (b) in contact. 7

Figure 6. Principal current conduction mechanisms in metal semiconductor junctions. . 9

Figure 7. J-V characteristics exhibit Schottky rectification at the (a) graphene/n-Si (b) graphene/n-GaAs, (c) graphene/n-4H-SiC and (d) graphene/n-GaN interfaces 10

Figure 8. Energy band diagram of graphene (a) thermal equilibrium (b) forward bias and (c) reverse bias condition.. 11

Figure 9. Graphene/Si Schottky diode of Ref. 53. I–V characteristic of graphene/n-Si Schottky diode with and without uniform illumination of the graphene layer by a 30 mW, 532 nm wavelength laser (the inset shows the current on log scale).. 13

Figure 10. Solar cell with films of graphene on n-Si (a) I–V characteristics of two devices (0.1 cm^2 and 0.5 cm^2) showing excellent rectification. The insets show the ideality factor and the series resistance of the 0.1 cm^2 cell extrapolated from the forward linear region (b) Solar cell parameters (J_{SC}, V_{OC}, FF and η) vs. light intensity for the 0.1 cm^2 Gr/n-Si heterojunction 14

Figure **Page**

Figure 11. (a) Full spectral responsivity of the Gr/Si photodetector before and after Al_2O_3 coating (b) Multi-cycle photocurrent responses to pulsed picoseconds UV laser with a wavelength of 375 nm, at V_b = 0.0 V........... 15

Figure 12. (a) J–V characteristics of the Gr/Si Schottky junction for various illumination power. (b) Photoresponse of the Gr/Si heterojunction photodetector for various light intensities at self-powered mode, and the transient photoresponse of the Gr/Si Schottky junction diode under 532 nm laser illumination. 16

Figure 13. (a) CVD graphene production setup: The furnace has a quartz tube to heat up the substrates at 1100 ºC. Thermocouple is used to control temperature, and flowmeters are used to control gas flow. (b) Cu foils were diced into small pieces prepared for graphene growth. (c) Cu foils are placed on quartz wafers in the furnace. 17

Figure 14. Heating (1), annealing (2), growth (3) and cooling (4) stages of graphene growth process on Cu foil with schematic representations by CVD. 18

Figure 15. Schematic illustration of the graphene transfer process. (a) CVD grown graphene on Cu. (b) Photoresist was drop casted onto graphene/Cu substrate. (c) Then,PR/graphene substrate was immersed in FeCl3 solution. (d) After Cu was completely etched, PR/graphene was transferred onto the device structure (e-f). 19

Figure 16. The schematic of device structures of Gr/Si Schottky diodes. 20

Figure 17. Raman spectroscopy measurement setup (Monovista-Princeton instruments in Physics Department, IZTECH. 22

Figure 18. Raman spectra of single layer, bilayer and few layer graphene 23

Figure 19. Band diagram of tip and sample in KPFM. 24

Figure 20. AFM setup in Quantum Device Laboratory, Physics Department at IZTECH. 25

Figure 21. Laboratory at IZTECH. (b) The photocurrent spectroscopy setup; a quartz tungsten halogen lamp (Osram, 275 W) (1), a high resolution monochromator (Newport, Oriel Cornerstone) (2), flame spectrometry (Oceans Optics) (3). a closed loop cryostat (4). 26

Figure 22. Picture of the sample after mounted onto the sample holder of cryostat. 27

Figure **Page**

Figure 23. (a) Configuration for four probe Van der Pauw electrical conductivity measurement (graphene touches the contacts representatively). (b) Device configuration of four probe Cr/Au contacts on SiO_2 and graphene touching contacts on n-Si substrate. 28
Figure 24. (a) The probe station setup. (b) The probes which are connected independently of each other and the holder has ability to move x,y and z directions. (c) The probe station setup with led integrated z- stage and (d) while led is on the device during Hall effect measurement. 29
Figure 25. (a) The photograph of graphene/Si device and optical image collected from different regions of the sample (scale bar is 40 μm) and (b) Raman spectra of CVD graphene (CVDG) collected from different regions of the sample. 30
Figure 26. Contact potential differences of HOPG and CVDG on n-Si. 31
Figure 27. (a) Schematics of Gr/n-Si device structure and (b) J-V characteristics of Gr/n-Si and ER/Gr/n-Si devices under dark. 32
Figure 28. dV/dln (I) vs I and H(I) vs I plots of Gr/n-Si Schottky diode. 33
Figure 29. J-V characteristics of (a) Gr/n-Si and (b) ER/Gr/n-Si devices under dark and 850 nm light with illumination power density of 25 $\mu W/cm^2$ 35
Figure 30. J-V characteristics of (a) Gr/n-Si and (b) ER/Gr/n-Si devices in semi-logaritmic scale under dark and 850 nm light with illumination power density of 25 $\mu W/cm^2$. 35
Figure 31. Photoswitching behavior of the Gr/n-Si and ER/Gr/n-Si photodiodes under 850 nm light with illumination power density of 25 $\mu W/cm^2$ at zero bias. 36
Figure 32. UV-Visible Spectrum of Epoxy Resin (ER). 37
Figure 33. Responsivity of Gr/n-Si and ER/Gr/n-Si photodiodes at zero bias. 39
Figure 34. Time dependent responsivity measurements of Gr/n-Si and ER/Gr/n-Si photodiodes. 39
Figure 35. (a) I-V plot of the CVDG/n-Si device on a logarithmic scale in the dark and under illumination under various P_i of 15, 30, 50, 100 and 180 $\mu W/cm^2$, respectively and (b) The graph of P_i dependent V_{oc} and I_{sc} of the device (under self-powered conditions). 40

Figure **Page**

Figure 36. (a) Cross-section of Gr/n-Si heterojunction diode, (b) Schematic energy band diagram of the Gr/Si interface under dark and light illumination. The tunable V_{oc} with respect to the light illumination is clearly depicted and the red and blue arrow shows the direction of the movement of holes and electrons, respectively. 42

Figure 37. The graph of illumination power density dependent average carrier concentration and mobility of the Gr/n-Si device (at self-powered mode). 43

Figure 38. The graph of SBH (ϕ_B) differences with respect to different Pi values (inset shows the KPFM measurements of CVDG and HOPG. HOPG (black color) is used as reference). 43

LIST OF TABLES

Table **Page**

Table 1. Optimized graphene growth parameters on Cu foil by CVD. 18

Table 2. Ideality factor (η) and Schottky Barrier Height (ϕ_B) of the Gr/n-Si diodes. 34

LIST OF ABBREVIATIONS

CVD……………………………………………………………Chemical Vapor Deposition

KPFM…………………………………………………Kelvin Probe Force Measurement

PS……………………………………………………………..Photocurrent Spectroscopy

CHAPTER 1

INTRODUCTION

Graphene, two-dimensional carbon material which is very attractive due to its remarkable properties such as very high charge carrier mobility, high optical transparency, large surface-to-volume ratio[1] and high sensitivity through adsorbates [2]. These amazing properties and characteristics make graphene a promising material for electronic and optoelectronic applications. So far, there have been made a great effort to obtain the device that combines graphene and semiconductor to enhance device performance and functionality. Schottky diode is one of the devices obtained by incorporation of graphene with semiconductors.

Schottky diode is a device which operates on the basis of transport across metal/semiconductor junction that can work in photovoltaic mode (at zero bias or self-powered) and in photoconductive mode (under reverse bias) [3]. In structure of graphene based Schottky diodes, graphene is changing place with metal as Schottky electrode[4–7]. Graphene/semiconductor junction is similar to metal/semiconductor junction where a potential energy barrier is formed at the interface. The potential barrier causes rectifying behavior in the current-voltage (I-V) characteristics of the Schottky diode. Unlike conventional metal/semiconductor junction, the potential barrier height of the graphene/semiconductor junction can be tuned as a result of the modification of graphene's work function (Φ_G) [8,9]. The modification can be done by through chemical doping [10], temperature [11], desorption and adsorption of atmospheric adsorbates [12] and electrostatic gating [13]. For photodetectors and solar cells, manipulation of electrode work function is essential to improve the device efficiency. However, for stable device operations, graphene must be encapsulated with a proper material or the measurements should be taken under vacuum conditions.

This thesis focused on electrical and optoelectronic characteristics of CVD grown p-type graphene and n-Si (Gr/n-Si) forms Schottky junction photodiode which can operate at a wide spectral wavelength range between 390 and 1100 nm at photovoltaic (self-powered) mode.

In the first part of the thesis, Gr/n-Si Schottky device was encapsulated with Epoxy Resin (ER) to prevent graphene from atmospheric adsorbates and to investigate stability of the device in terms of photoresponsivity. The electronic and optoelectronic characterizations of Gr/n-Si photodiodes were done before and after coating the devices with ER. Time-resolved photocurrent spectroscopy measurements showed that the devices exhibit enhanced photodetector performance in terms of photo-switching characteristics, spectral responsivity.

In the second part, light induced manipulation of the Schottky barrier height of Gr/n-Si photodiode is studied. Measurement of Φ_G were done by Kelvin Probe Microscopy (KPFM) in the dark. The electrical measurement of the device taken under light illumination indicated the alteration of the work function of the CVDG/n-Si heterojunction. Furthermore, Hall Effect measurements of graphene on n-Si substrate showed that the sheet carrier density of graphene was increased as a function of illumination power.

1.1. Graphene

Graphene, as a two-dimensional material which is comprised of an thin layer has atomic thickness of sp^2-bonded carbon atoms placed in a honeycomb structure. Three covalent bonds are formed in the plane by the hybridization of $2s$ orbital with the $2p_x$ and $2p_y$ orbitals with angle of 120°. In graphene, p_z orbital is perpendicular to the plane and constitutes a weak π-bond. The bonding between p_x and p_y electrons is called σ bonding [2].

The π-bonds are not localized and are in charge of electronic conduction in the graphitic structures. The honeycomb structure of the graphene is realized by three strong covalent σ-bonds formed by each atom in plane a = 1.42 Å distance. One electron per atom forms the π -bonds and the electronic properties of graphene result from the π -electrons at low energies.

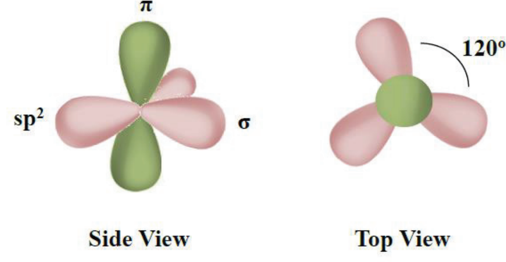

Figure 1. Schematic illustration of sp^2 hybridization in graphene unit cell [14].

Contrarily, energy bands far from the Fermi energy caused by the σ electrons. The graphene crystal structure (see Figure 2) can be seen as a triangular Bravais lattice with a two-atom basis (an atom for each sublattice, the so-called A and B sublattices); a_1 and a_2 can be written as

$$a_1 = a(\frac{3}{2},\frac{\sqrt{3}}{2})\ ,\ a_2 = a(\frac{1}{2},-\frac{\sqrt{3}}{2}) \tag{1.1}$$

The reciprocal lattice vectors are; $b_1$and b_2 can be written as;

$$b_1 = \frac{2\pi}{a}(\frac{1}{2},\frac{\sqrt{3}}{2})\ ,\ b_2 = \frac{2\pi}{a}(\frac{1}{2},-\frac{\sqrt{3}}{2}) \tag{1.2}$$

Figure 2. (c) shows the first Brillion zone of graphene. Γ and M are called as the zone center and the midpoint, respectively. K and K' are the two nonequivalent corners of the first Brillion zone the position is expressed as

$$K = \frac{2\pi}{3a}(1,\frac{1}{\sqrt{3}})\ ,\ K' = \frac{2\pi}{3a}(1,-\frac{1}{\sqrt{3}}) \tag{1.3}$$

In particular, the corners of Brillion zone (K and K') are considerably important. As the outstanding physics of graphene resulted at these corners that are called as Dirac points. At these Dirac points, that have two different sets. Each of them is nonequivalent and included three Dirac points.

Fermi level of undoped graphene lies completely at the Dirac points, and hence graphene can be regarded as a gapless semiconductor or a zero-overlap semimetal. The electron dispersion (k) around the Dirac points is linear instead of parabolic as most of semiconductors. The linear dispersion, as opposed to the ordinary parabolic dispersion relation with a mass dependence, ($E=\hbar^2k^2/2m$), signs that the charge carriers move with a velocity that is independent of the energy, therefore behaving as relativistic and massless particles (Dirac fermions) with velocity (V_F).

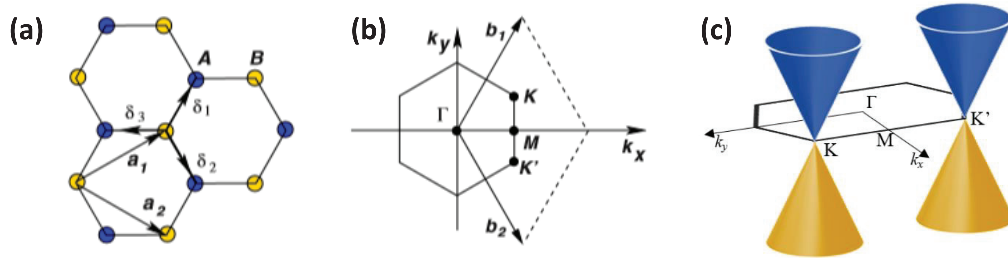

Figure 2. (a) Honeycomb lattice structure of graphene. The unit cell consists of two atoms labeled A and B, the lattice vectors are a_1 and a_2. (b) First Brillouin zone of graphene with reciprocal lattice vectors b_1 and b_2 as a function of k_x and k_y and (c) Brillouin zone of graphene with representation of Dirac cones near the K and K' points [14,15].

As a consequence, transport properties of the electron are described by the Dirac's equation, with several (relativistic) quantum mechanical effects [1,16–18] such as the unusual half-integer quantum Hall effect [17], Klein tunneling effect [18], minimum conductivity [2], and Veselago lensing [19].

The Fermi energy can be expressed in terms of carrier density n as $E_F = \hbar V_F \sqrt{\pi n}$ which refers that it is possible to tune the Fermi energy by changing the carrier density (both electrons and holes) by means of a bias gate in a graphene based field effect transistor. In graphene electrons or holes can be majority carriers based on the position of the Fermi energy with respect to the Dirac point (see Figure 3). The manipulation of the Fermi level is possible by changing majority of n or p type carrier transport (ambipolar

effect). From these expressions, the carrier density is zero at T = 0 K. For T > 0 K, there is a non-zero carrier density.

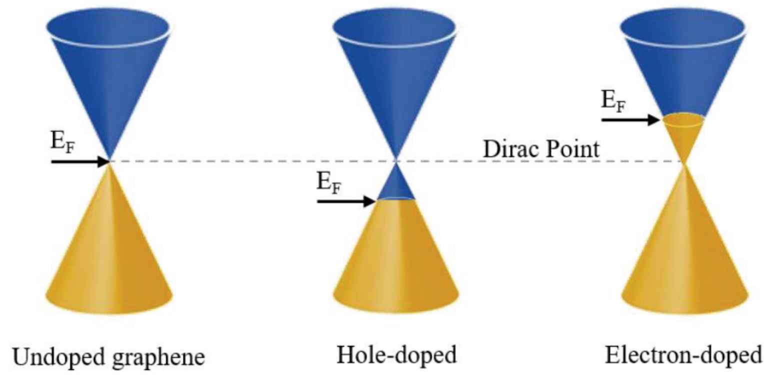

Figure 3. Linear dispersion (Dirac cone) representation with conduction and valence bands through the *K* point (Dirac point). With charge transfer to or from the graphene leads electron or hole doping which replaced the Fermi Level above or below to the Dirac point [15].

While graphene can be prepared by using mechanical exfoliation method [20], epitaxial growth on SiC [21,22], chemical exfoliation [23], chemical vapor deposition (CVD) has appeared as an essential way for the preparation and production of graphene since it was first reported in 2008 and 2009 [24–28]. However, from a practical point of view, exfoliation and epitaxial growth are viable for industry-scale production. Graphene produced by CVD is therefore of greater interest. It is known from the literature that graphene layers grown by CVD has strong p-type carrier density [29,30] since therefore its fermi level is below Dirac point [31–33]. At room temperature, the theoretical limit of graphene's carrier mobility is about 2×10^5 cm^2/V·s at carrier densities on the order of a few 10^{12} cm^{-2} [34,35]. This predicted high mobility is experimentally obtained at room temperature; 2.5×10^5 cm^2/V·s was determined by Hall measurement on exfoliated graphene sandwiched in hexagonal boron nitride (h-BN) sheets [36] under a low carrier density of about 10^{11} cm^{-2}. For CVD graphene transferred onto SiO2 and hexagonal boron nitride surfaces, the carrier mobility maxima obtained at room temperature are 1.6 $\times 10^4$ and 3×10^4 cm^2/V·s, respectively [37,38]. The hole concentration of CVD grown

graphene is about 10^{12} cm^{-1} [39–41] and by doping the hole concentration can be increased up to about 10^{13} cm^{-1} [42].

Graphene's zero bandgap and the perfectly symmetrical energy band structure lead to its extraordinary optical properties. In theory, a single layer of graphene absorbs $\pi\alpha \approx 2.3$ % of light regardless of the wavelength, where α is the fine-structure constant. This universal absorption has been experimentally established on suspended exfoliated graphene [43]. UV-Visible-NIR spectrum of the graphene in Figure 4 shows an excellent optical transparency in the ultra-violet and the visible regions. Hence, this property makes graphene a perfect candidate to be used as transparent conductive electrode (TCE) for optoelectronics applications. Conventionally, current research uses Ni/Au, Ti, TiW and indium tin oxide (ITO) based transparent conductive electrodes for solar cell and photodetector applications.

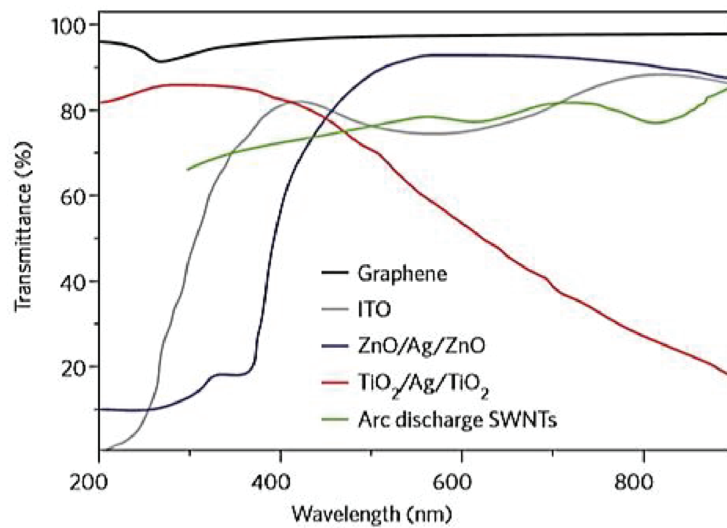

Figure 4. The optical transmittance of transparent conductive electrodes that are used commercially for UV, visible and NIR regimes [44].

As seen in Figure 4 The optical transparency of these metal electrodes. The transmittance of transparent conductive electrodes which are used in a commercial way for UV, visible and NIR regimes [44]. This means, graphene is an unique candidate to be performed as transparent conductive electrode both in photovoltaic devices and

photodetectors that are meant to work in the UV-vis region, as this 2D material has a transparency of over 90 percent in the region between 200-900 nm.

1.2. Physics of Schottky Junction

A metal-semiconductor (M/Sc) junction exhibiting rectifying behavior is known as a Schottky barrier junction. M/Sc contacts exhibit rectification characteristics because of the existence of an electrostatic potential barrier between the metal and the semiconductor, which is due to the difference in work function between the two materials. Figure 5 illustrates the energy band diagrams of an isolated n-type semiconductor and a metal. Here the work function of the metal ϕ_m is greater than that of the semiconductor. Work function is defined as the energy difference between the vacuum level and the Fermi level. For a semiconductor, the work function is equal to $\chi+\phi_{bn}$, where χ is the electron affinity and ϕ_{bn} is the difference in energy between the conduction band and the Fermi level [45].

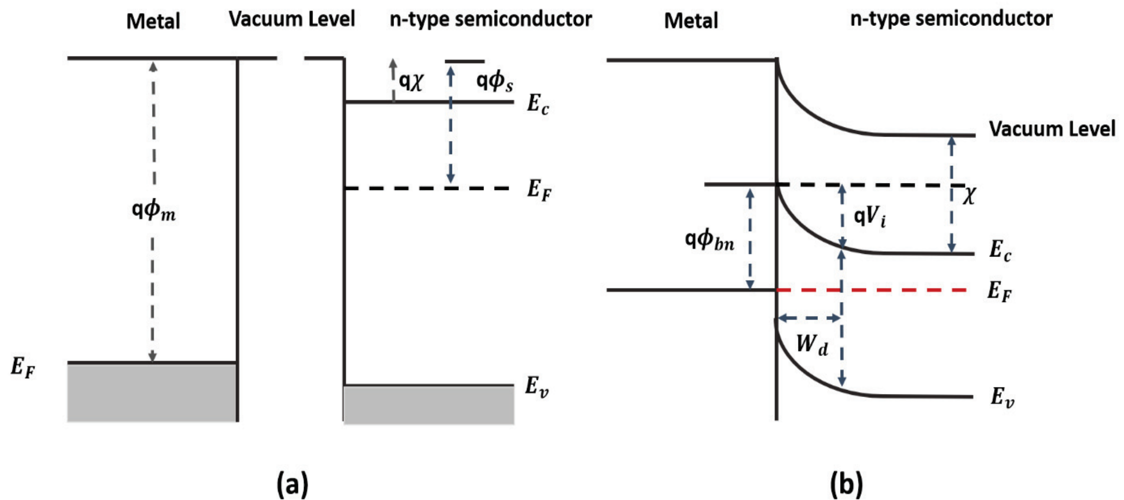

Figure 5. Ideal Metal/n- type semiconductor band diagram (a) Seperate and (b) in contact.

When a metal and an n-type semiconductor are brought together and if the work function of the metal is greater than the work function of the semiconductor, electrons will flow from the semiconductor to the metal until the Fermi levels align. As they are brought closer, an increasing negative charge is built up at the metal surface with an equal and opposite charge in the semiconductor, creating an electric field in the junction [46]. This built-in potential opposes the flow of electrons and eventually forces a state of equilibrium to be obtained. Since the carrier concentration in the semiconductor is much less than the concentration of electrons in the metal, the positive charges in the semiconductor form a layer and the bands of the semiconductor near the interface bend upwards [47].

As the metal and an n-type semiconductor are brought into close contact with each other, the barrier height ϕ_{bn} formed between the metal and the n-type semiconductor, ϕ_{bn}, is expressed ideally by the Schottky Mott model, given by:

$$q\phi_{bn} = q(\phi_m - \chi) \tag{1.4}$$

In the case of a p-type semiconductor, the barrier height, ϕ_{bp}, is given by:

$$q\phi_{bp} = E_g - q(\phi_m - \chi) \tag{1.5}$$

The Schottky Mott model states that the barrier height can be controlled by the choice of the metal. If there is a large density of interface states present at the metal semiconductor interface, then the barrier height is defined by the Bardeen model where the barrier height is only determined by the interface state density [48]. Experimental results sit somewhere between two models for real Schottky diodes.

The current transport in metal-semiconductor contacts is mostly governed by the majority charge carriers, unlike the minority charge carriers are responsible in p-n junctions. Four fundamental transport processes can be seen on Figure 6 under forward bias, the reverse processes occur in case of reverse bias [47]. Those processes are; (1) emission of electrons from the semiconductor over the top of the barrier into the metal (this process is known to be dominant for moderately doped semiconductors at certain temperatures), (2) quantum-mechanical tunneling of electrons through the barrier which is critical for heavily doped semiconductors and responsible for ohmic contacts, (3)

recombination in the depletion region, like observed in a p-n junction, (4) electron diffusion in depletion region. For high mobility semiconductors the transport can be described by the thermionic emission theory.

The thermionic emission theory (TE) is known as the carriers on a surface are released due to the thermal energies they gain. In the Schottky contacts the TE is known as the case of carriers gaining sufficient thermal energy are transferred from semiconductor to metal or from metal to semiconductor over the potential barrier. When voltage is applied to the metal/semiconductor (M/Sc) contact, the Fermi levels in the metal and semiconductor do not remain at the same level as in the thermal equilibrium. The barrier height for electrons on the metal side of these M/Sc contacts does not depend on the applied voltage. However, the barrier height for electrons on the semiconductor side decreases with the applied forward biased voltage and increases with the reverse bias voltage. Thus, the current from the semiconductor to the metal under the forward bias increases, but this current decreases in the case of reverse bias. This mechanism is provided by majority of carriers in Schottky diodes (by the electrons in metal / n-type semiconductor contacts and by the holes in metal / p-type semiconductor contacts). According to TE theory as follows (1) the system barrier height is much higher than thermal energy of system (kT/q), (2) the system is thermally under equilibrium at the interface and (3) thermal equilibrium of the system does not affected by charge accumulation at the interface [49].

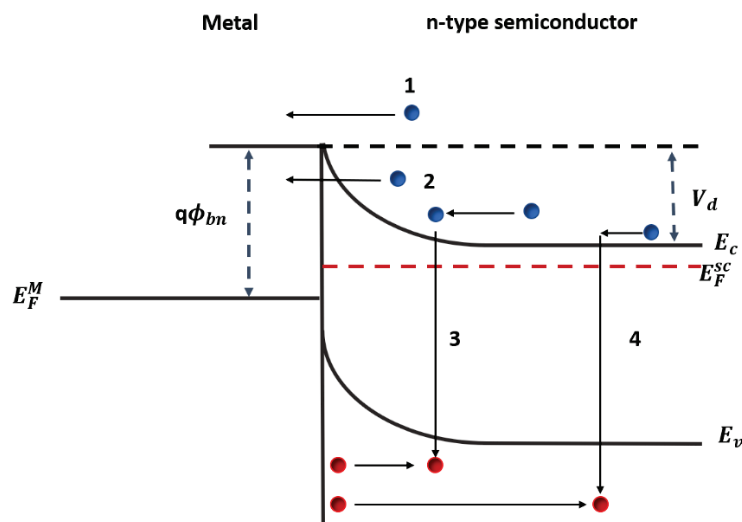

Figure 6. Principal current conduction mechanisms in metal semiconductor junctions.

The current mechanisms in metal-semiconductor contacts were first proposed by Bethe and more specifically by Crowell and Sze [50]. The current density can be written as indicated below;

$$J = J_0 \left[exp\left(\frac{qV_D}{\eta kT}\right) - 1 \right] \tag{1.6}$$

In this expression ; q is the electron charge, k is the Boltzmann constant, T is the absolute temperature, V_D is the applied potential , η is the ideality factor and

$$J_0 = AA^* exp\left(-\frac{q\phi_B}{kT}\right) \tag{1.7}$$

where A is area of diode, ϕ_B is Schottky barrier height and A^* is Richardson constant.

1.3. Graphene/Semiconductor Heterojunction

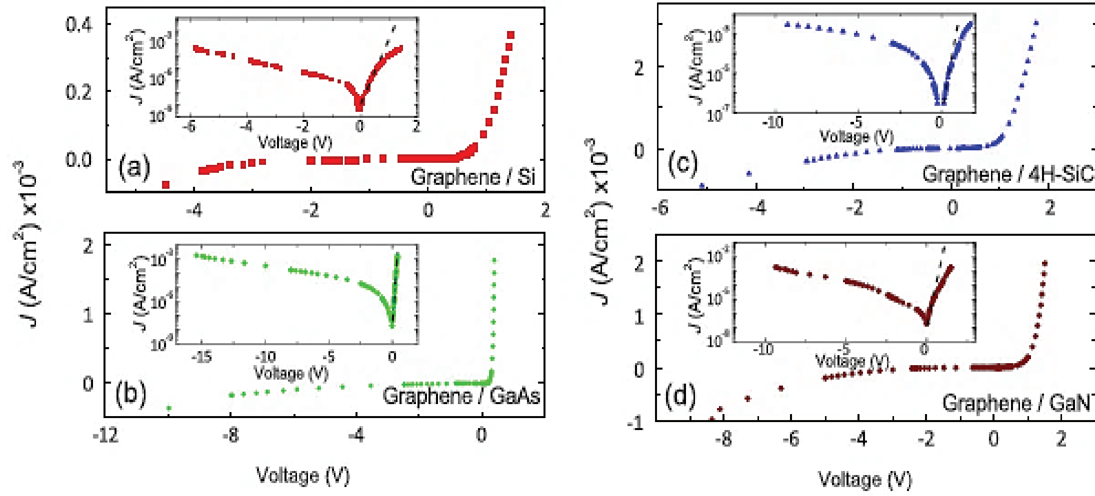

Figure 7. J-V characteristics exhibit Schottky rectification at the (a) graphene/n-Si (b) graphene/n-GaAs, (c) graphene/n-4H-SiC and (d) graphene/n-GaN interfaces [4].

Recently Schottky diodes with the metal replaced by graphene monolayers have attracted enormous interest. Graphene forms a Schottky junction when it is transferred

onto the surface of semiconductors such as Si, GaAs and SiC which have technologically importance [5,51]. Due to the fact that the graphene/semiconductor (G/Sc) heterojunction is expected to exhibit a strong rectification which can be used for Schottky barrier devices like tunneling field effect transistors and photodetectors with relatively low leakage currents [52].

Tongay et al. [4] showed that graphene forms Schottky junction with rectification behavior when it is transferred onto most of the conventional semiconductor materials like Si, GaAs, SiC and GaN (See Figure 7). They also found that the Fermi level of graphene is variable during the charge transfer at the G/Sc interface. These variations realize under reverse bias voltages when the amounts of electrons induced in the graphene which caused to increase the Fermi level of graphene and leakage current. In addition, the extracted Schottky Barrier Height (SBH) values are determined by J-V (Arrhenius plot) on various G/Sc junctions.

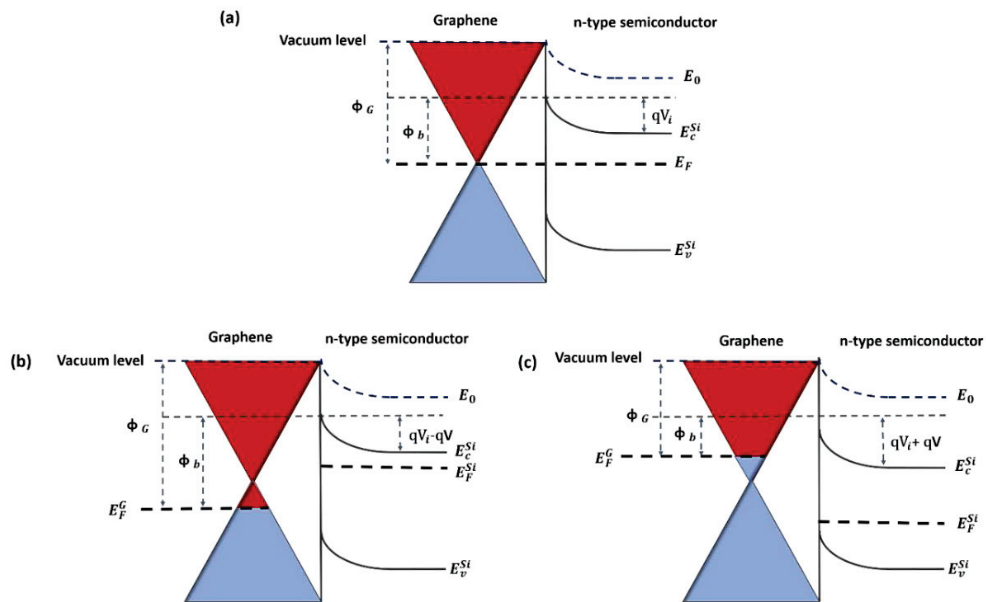

Figure 8. Energy band diagram of graphene (a) thermal equilibrium (b) forward bias and (c) reverse bias condition.

Unlike well-known M/Sc interface, in which the Fermi level of metal stays constant due to the high density of states, even small variation in charge carrier density can significantly manipulate the Fermi level of graphene. S.Tongay et.al [4] has suggested that

modification to the thermionic emission theory for taking into account the variation of the Fermi level in graphene owing to an applied bias. Conventionally in a metal-semiconductor interface, the charges induced in the metal by the semiconductor are negligible, as a result of the high density of states in the metal. For graphene the effect of induced charges is instead no longer negligible.

Figure 8 shows the Fermi level is at the Dirac point when there is no applied bias and the interface between graphene and a n-type semiconductor. Under forward bias, the Fermi level in graphene (E_F) is shifting downwards, because fewer charges are required to transmit positive charges formed in the depletion layer of the semiconductor. Conversely, under inverse bias, the depletion layer in the semiconductor increases and the number of negative charges in the graphene increases, thereby causing the E_F to shift upwards.

1.4. p-type Graphene/n-Si Heterojunction

When graphene (Gr) is transferred onto Si, the resulted graphene/silicon (Gr/Si) heterostructure exhibits an obvious Schottky behavior. [53] Due to high optical transparency and conductivity properties of the Gr, Gr/Si heterostructures exhibit fascinating optoelectronic properties and have been developed for high-performance solar cells and photodetectors [54–57]. In general, Gr/Si heterojunction is fabricated [51] by transferring p-type CVD graphene onto n-type Si substrate [58]. When the contact between graphene and Si is established, charge transfer occurs until the respective Fermi levels align for the inequality in their work functions. In consequence of the formation of Schottky barrier at the Gr/Si interface, partial carriers in Si substrates show a tendency to move to the graphene side and eventually, the energy levels near the Si surface will bend upward (for n-Si) causing the formation of depletion region and built-in electric field near the Gr/Si interface.

Gr/Si Schottky photodiode can function under both photovoltaic mode (at zero bias or self-powered) and photoconductive mode (under reverse bias). A lot of research have been focused on Gr/Si heterojunction showing good performance as self-powered photodetector [3,59] and has many applications as solar cell . When Gr/Si junction is put

under light illumination, the Si substrate absorbs the photons with energy higher than the bandgap and generates electron–hole pairs (also called exciton). In the depletion zone, photo-generated excitons are quickly separated by the built-in field of Gr/Si heterojunction. Excessive holes move toward the anode (Gr), and electrons toward the cathode (Si). As a result, leading to a sizeable photocurrent. This phenomenon is known as photovoltaic effect [60]. As mentioned previously, electrons and holes accumulate in different parts of Gr/Si junction when it is illuminated. The accumulation of carriers gives rise to a photo-voltage that is counter to built-in electric field. In the case of open circuit, the photo-voltage eventually reaches a maximum and gives to an open circuit voltage (V_{OC}). On the other hand, all the carriers move through the external circuit if the photodiode is short-circuited, generating a maximum current density called as short circuit current (J_{SC}).

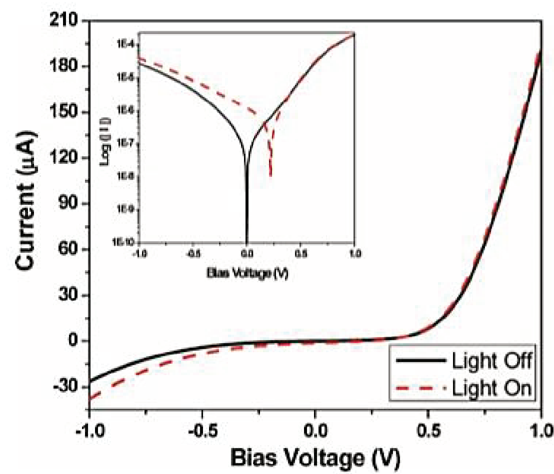

Figure 9. Graphene/Si Schottky diode of Ref. [53]. I–V characteristic of graphene/n-Si Schottky diode with and without uniform illumination of the graphene layer by a 30 mW, 532 nm wavelength laser (the inset shows the current on log scale).

C.C. Chen et al. [53] has showed that the rectification behavior of Gr/n-Si heterojunction under dark and while 30 mW, 532 nm laser light was uniformly shining on graphene. The increase in current and the occurence of an V_{oc} (as can be seen more clearly in the inset of Figure 9) show photoexcitation of charge carriers and generation of photocurrent. Due to its optical transparency of the graphene layer, incident laser light is

expected to be absorbed in the Si substrate, where it generates the photocurrent observed under reverse conditions.

The photovoltaic effect in the Gr/n-Si junction had been previously reported and studied in Ref. [56], with films of graphene sheets, synthesized by CVD method (see Figure 10). The I–V characteristics of the devices were highly rectifying and photovoltaic parameters of the cell (J_{sc}, V_{oc}, Fill Factor (FF), and Ideality Factor (η)) has been showed as functions of the incident light intensity. J_{sc} is linearly dependent on the light-intensity incident on the cell, consistent with increment in photogenerated carriers. V_{oc} shows a similar trend. FF and η decrease monotonically with an increase in the light intensity.

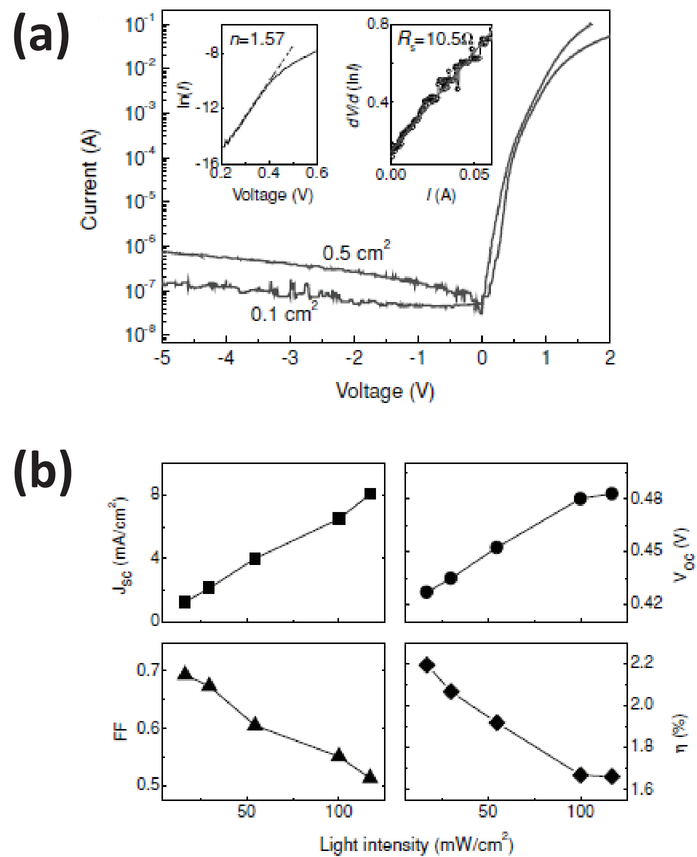

Figure 10. Solar cell with films of graphene on n-Si (a) I–V characteristics of two devices (0.1 cm^2 and 0.5 cm^2) showing excellent rectification. The insets show the ideality factor and the series resistance of the 0.1 cm^2 cell extrapolated from the forward linear region (b) Solar cell parameters (J_{sc}, V_{oc},, FF and η) vs. light intensity for the 0.1 cm^2 Gr/n-Si heterojunction [56].

To manipulate V_{oc} of Gr/n-Si junction means that the barrier height and work function (WF) of graphene also change due to fermi level difference. Manipulation of V_{oc} in Gr/Si photodiode structure is determined by incident illumination power dependence [3,58], temperature [11] and time dependent light exposure [61]. Moreover, it is possible to measure WF is from the contact potential difference (CPD) measured using Kelvin probe force microscopy (KPFM) [62].

The photoresponsivity and response time of the Gr/Si photodetector which are one of the most important parameters for evaluate the performance of a photodetector. Responsivity is defined as the ratio of photocurrent to incident light power, in a unit of A/W that indicates how efficiently a photodetector responds to an optical signal. The response of a photodetector to an optical signal is characterized by the rise/fall times which are strongly related to the charge transport/collection and the bandwidth of the photoresponse. Xia Wan et. al. [59] has presented Gr/Si photodetector in the near-ultraviolet and mid-ultraviolet spectral region, exhibits high performance at self-powered mode with high photoresponse as 0.2 AW^{-1} and with fast time response (5 ns) (see Figure 11).

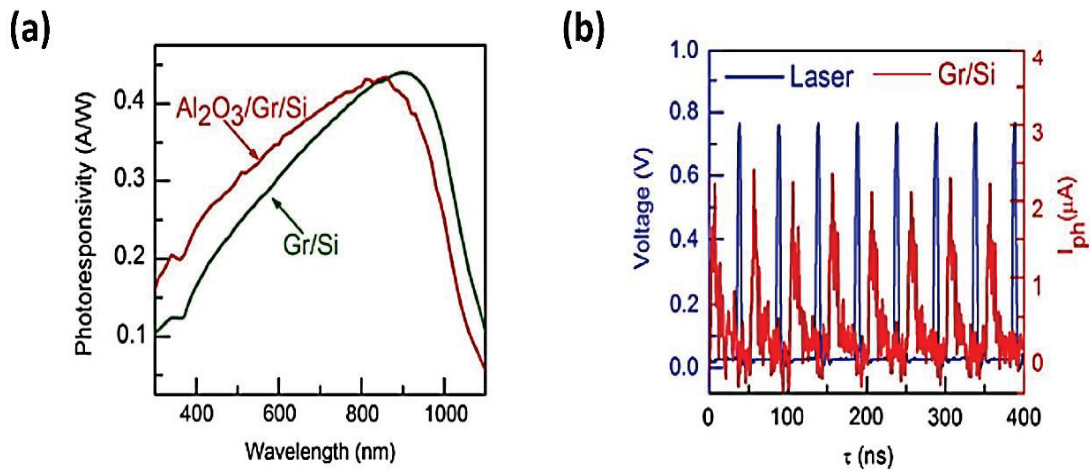

Figure 11. (a) Full spectral responsivity of the Gr/Si photodetector before and after Al_2O_3 coating (b) Multi-cycle photocurrent responses to pulsed picoseconds UV laser with a wavelength of 375 nm, at $V_b = 0.0$ V [59].

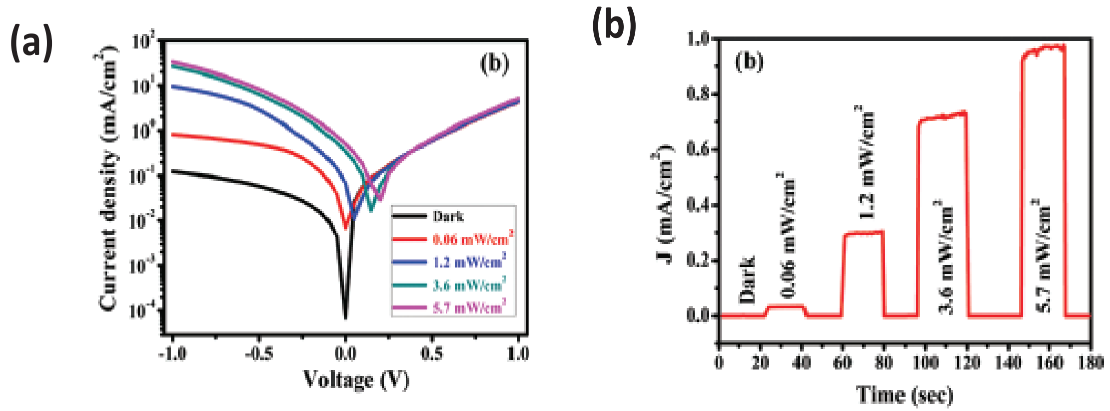

Figure 12. (a) J–V characteristics of the Gr/Si Schottky junction for various illumination power. (b) Photoresponse of the Gr/Si heterojunction photodetector for various light intensities at self-powered mode, and the transient photoresponse of the Gr/Si Schottky junction diode under 532 nm laser illumination [3].

Dharma et. al. [3] has showed that The Gr/Si heterojunction exhibits outstanding Schottky diode characteristics and investigates under different illumination power. The Gr/Si heterojunction has a barrier height of 0.76 eV and shows good performance as a self-powered photodetector which responds to 532 nm wavelength light at zero bias. The self-powered photodetector works under the mechanism of photovoltaic effect and shows responsivity as high as 510 mA W^{-1} and its photo switching ratio is 10^5 with a response time of 130 ms.

Passivation and protection of the Gr/Si interface are also important to stabilize photoresponse of the junction. Device stability is crucial for utilization in industrial applications. The performance of Gr/ Si heterojunction is highly affected by the high recombination at Gr/Si interface and the continues but non-uniform growth of native oxide that prevents the tunnelling of the photo-generated charge carriers and leading to performance degradation and instability issues [63–65]. Encapsulation of the Gr/Si heterojunction interface with a proper material which has high optical transmittance prevents the interaction with air and allow optoelectronic applications. At this point, epoxy resin appears as one of the suitable material for encapsulation according to the literature [66,67].

CHAPTER 2

EXPERIMENTAL

2.1. Growth of Graphene by CVD Method

Chemical Vapor Deposition (CVD) is one of the most preferred method in the synthesis of graphene since it provides an advantage in the production of high quality monolayer graphene. This method is vapor-phase process which is realized by placing transition metal films such as Cu [68], Ni [69], Pt [70] or Ir [71] in the atmosphere of a gas phase carbon (C) source precursor (CH_4, C_2H_4 etc.) in the CVD furnace under different temperatures (between 800 ^oC and 1100 ^oC). Then graphene layers are obtained by thermally cracking of C atoms on the transition metal substrate.

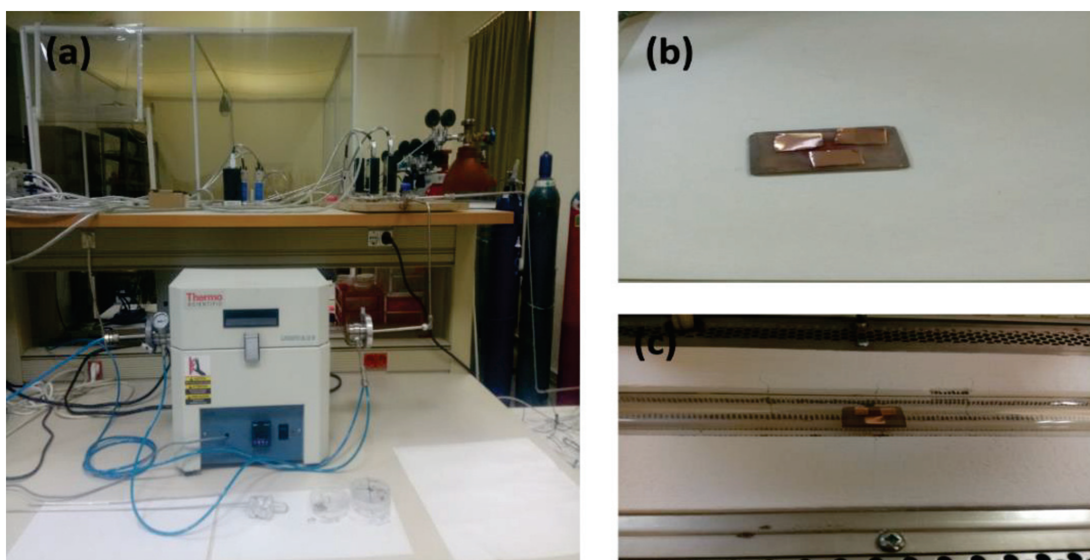

Figure 13. (a) CVD graphene production setup: The furnace has a quartz tube to heat up the substrates at 1100 ^oC. Thermocouple is used to control temperature, and flowmeters are used to control gas flow. (b) Cu foils were diced into small pieces prepared for graphene growth. (c) Cu foils are placed on quartz wafers in the furnace.

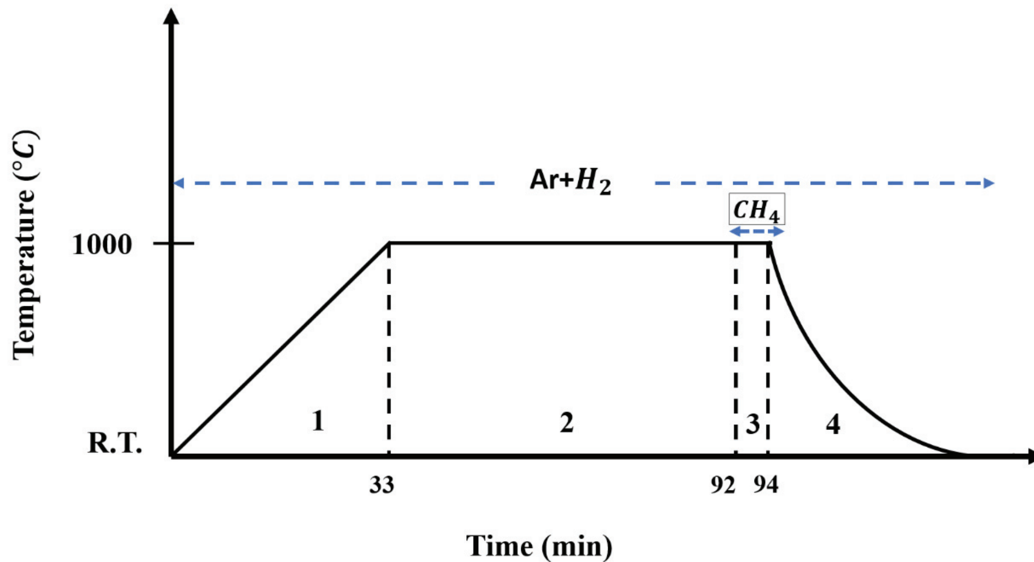

Figure 14. Heating (1), annealing (2), growth (3) and cooling (4) stages of graphene growth process on Cu foil with schematic representations by CVD.

As a catalyst-substrate material, Cu (25 µm thick, 99.8 % purity, Alfa Aesar) foil on the quartz plate was inserted to a tube furnace (Lindberg/Blue TF55035C Split Mini Tube). The process is performed in CVD system shown in Figure 13 (a).

Table 1. Optimized graphene growth parameters on Cu foil by CVD.

Temperature (°C)	**H_2 (sccm)**	**Ar (sccm)**	**CH_4 (sccm)**	**Ramp Time (min)**	**Annealing Time (min)**	**Growth Time (min)**
1000	20	1000	10	33	59	2

Figure 14 shows the four steps of growth process for CVD graphene. During the process Ar and H_2 were used to reduce the native oxide layer on the Cu foil. Here, as inert gas Ar is used to remove impurities on the Cu foil which increases the chamber pressure. In the first step, the process is started at the room temperature and the temperature is increased up to 1000 ^{o}C in 33 min. Then the Cu foil was annealed in order to increase the grain size of Cu foil under the same temperature and flows rates for 59 min. For the

growth stage, CH_4 gas was introduced into the tube furnace for 2 min to facilitate the graphene growth. Finally, for rapid cooling from growth temperature to room temperature the sample was left under gas flows of H_2 and Ar. All the parameters of the growth process are given in Table 1.

2.2. Transfer of Graphene on to SiO_2/n-Si Substrate

The steps of the graphene transfer methods are demonstrated in Figure 15. During the graphene transfer procedure Microposit S1318 Photoresist (PR) was utilized as supporting the graphene layer. The PR was drop casted on the graphene/Cu and then it is annealed in an oven at 70 °C overnight. Then, Cu foil was fully etched using Iron chloride ($FeCl_3$) solution to get suspend Gr/PR.

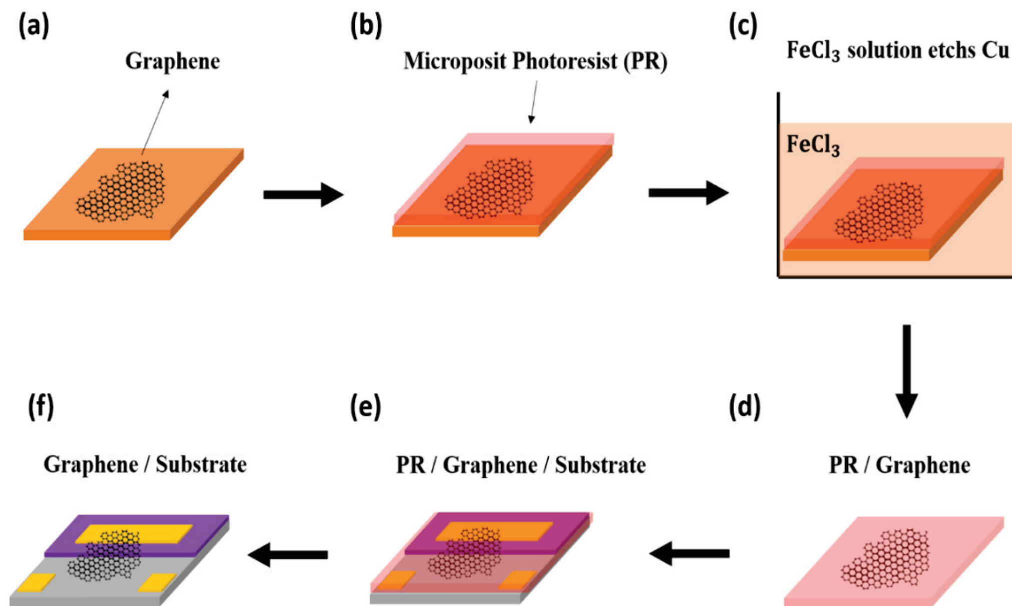

Figure 15. Schematic illustration of the graphene transfer process. (a) CVD grown graphene on Cu. (b) Photoresist was drop casted onto graphene/Cu substrate. (c) Then,PR/graphene substrate was immersed in $FeCl_3$ solution. (d) After Cu was completely etched, PR/graphene was transferred onto the device structure (e-f).

Thereafter, the PR/graphene was rinsed with deionized water (DI) to remove $FeCl_3$ residues. After drying the sample with N_2, the PR/ graphene was transferred onto the SiO_2/n–Si substrate. Next, the PR/graphene/substrate was heated on the hot plate at a temperature of 90 °C for 40 sec and 120 °C for 40 sec in order to adhere PR on to the substrate surface. At the end, the PR/graphene/substrate was rinsed with acetone for removing PR in order obtain graphene on the substrate.

2.3. Fabrication of Graphene/Silicon Schottky Devices

Commercial 10 mm x 10 mm sized SiO_2 (300 nm) /n-Si wafers with a resistivity of ρ = 1-10 Ω.cm were used as substrate. The substrates were ultrasonically cleaned for 15 min. in DI, acetone, ethanol and 2-proponal, respectively. Afterwards, a part of SiO_2 was etched using 3 % diluted HF for 15 min. in order to hinder electrical leakage along the graphene layer. Later, the graphene was transferred onto the sample to touch a portion of the Si and SiO_2. Area of the transferred graphene on n-Si substrate (active area of the device) is 3 mm x 3 mm.

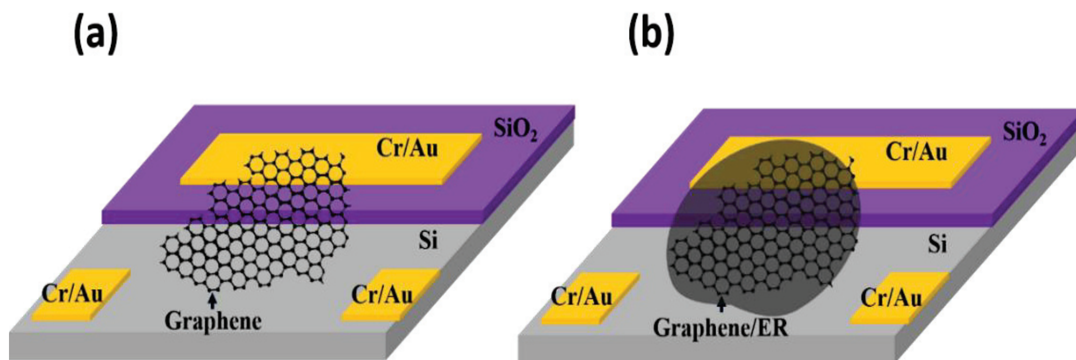

Figure 16. The schematic of device structures of Gr/Si Schottky diodes.

The electrodes of Cr (5 nm) and Au (80 nm) were deposited using Thermal Evaporation technique on SiO_2 and n-Si to get ohmic contact. As seen in Figure 16, also

Epoxy Resin (ER) was dropped on the graphene using drop casting method for encapsulating the graphene layer.

2.4. Characterization Techniques

2.4.1. Optical Microscopy

In an optical microscope, the object is illuminated by white light from the condenser and the reflected light forms an enlarged image of the sample through an objective lens. The light passing through the objective lens may be directed by a beam splitter into a lens for binocular observation or through a projection lens to a CCD camera. Optical microscopy is well established tool which can be used to analyze large area of graphene film on a substrate due to the obvious contrast difference between graphene and the substrate. Graphene can be selected from a Si/SiO_2 substrate since interference occurs between the reflection path of SiO_2 to Si and air to Si/SiO_2 interfaces [72,73].

An optical microscope Optika B-500 Optical Microscope is used for rapid observation of large area continuity (i.e., to determine whether there is a crack) and homogeneity (i.e., to determine whether the color of the graphene is the same all over) of graphene on the Si/SiO_2 device. In this thesis, optical microscopy is utilized for rapid observation of large area continuity (i.e., to determine whether there is a crack) and homogeneity (i.e., to determine whether the color of the graphene is the same all over) of graphene on the Si/SiO_2 substrate. This is known as Rayleigh scattering. Raman scatterings occur due to the inelastic scattered photons in material. Inelastic scatterings are divided into two as Stokes and anti-Stokes scattering. Stokes scattering process becomes when the frequency of the scattered photon is less than the frequency of the incident photon and the energy is added to the sample.

2.4.2. Raman Spectroscopy Measurement Technique

Raman spectroscopy is a technique which is used commonly to determine the number of graphene layers and their continuity and quality. Raman spectroscopy is a spectroscopic technique based on the inelastic scattering of monochromatic light from laser source. This method relies on the scattering of incident monochromatic light from an atom or molecule by interacting with the vibrational modes of the atoms in a crystal. Photons are elastically scattered from atoms or molecules which means that the kinetic energy of scattered and incoming photons is conserved. In anti-Stokes, the frequency of the scattered photon is greater than the frequency of the incident photon and a phonon is annihilated from the sample. Both shifts in the energy of incoming photon and this information help to examine the material properties [74]. Raman spectroscopy measurements were done in Physics Department, IZTECH Nanophotonics and Quantum Optics Laboratory as seen in Figure 17. Raman signals were recorded in a spectral range between 1000 – 3100 cm^{-1} using Ar^{+} ion laser 488 nm (2.54 eV) excitation (600 grooves/mm grating) to observe all D, G and G' peaks of graphene. The measurements were taken in combination with a 100x microscope objective. Each spectrum was analyzed using TriVista software.

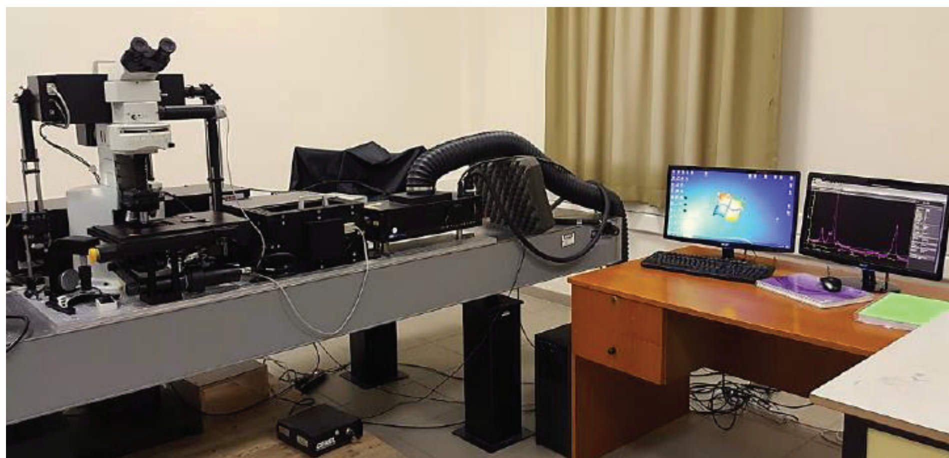

Figure 17. Raman spectroscopy measurement setup (Monovista-Princeton instruments) in Physics Department, IZTECH.

As mentioned in literature [75], there are some specific peak positions of graphene in Raman spectroscopy measurements. The characteristic peaks of graphene; D peak, G peak and 2D peak appears at 1350 cm^{-1}, 1580 cm^{-1} and 2675 cm^{-1}, respectively. D is related to the disorder due to the defects in sp^2 carbon systems. G peak reveals the vibration between C-C bonds. The other dominant peak is 2D peak. This peak is the second order process of D peak and used in the determination of graphene layer. The intensity ratio of G and 2D peaks give the number of layers of graphene.

If these peak ratios are;

$$\frac{G}{2D} = \frac{1}{2} \longrightarrow \text{single layer}$$

$$\frac{G}{2D} = 1 \longrightarrow \text{bilayer}$$

$$\frac{G}{2D} > 1 \longrightarrow \text{multilayer}$$

The characteristic peaks and related wavenumbers of graphene were determined in Raman spectroscopy measurements.

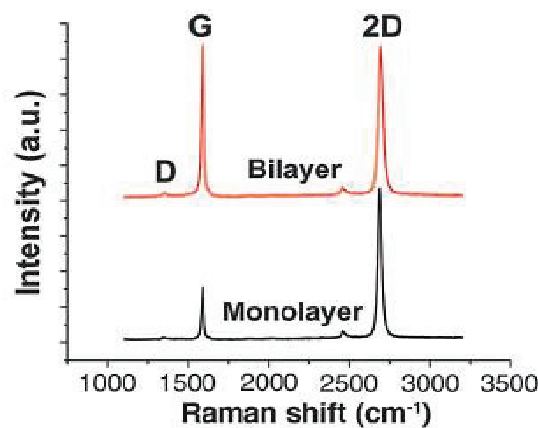

Figure 18. Raman spectra of single layer, bilayer and few layer graphene [76].

2.4.3. Kelvin Probe Force Microscopy

Kelvin probe force microscopy (KPFM), also known as surface potential microscopy, has been used in a diversity applications for metals, semiconductors and insulators. While KPFM measures the work function in conductive materials, while this method is used to measure the surface potential in non-conducting materials. Also, KPFM provides information about charge distribution and surface potential of semiconductor materials.

Because of the fact that KPFM was derived from available atomic force microscopy (AFM), there is an electrostatic interaction between conducting tip and the surface of material. If this surface is metal, there occurs an interaction between two metals, there are two different Fermi levels when these two metals touch each other, electron transfer begins to balance these Fermi levels. This is caused by the electron flow between these surfaces and named as the contact potential difference (CPD). By applying bias voltage or potential to the system, this electron flow and CPD balance is provided. This process is named as Kelvin method. Meanwhile, from the amount of applied external voltage, work function or surface potential of sample can be obtained can be seen in Figure 19 [77]. Since graphene is a semi-metallic material, it is possible to measure its work function on various substrates.

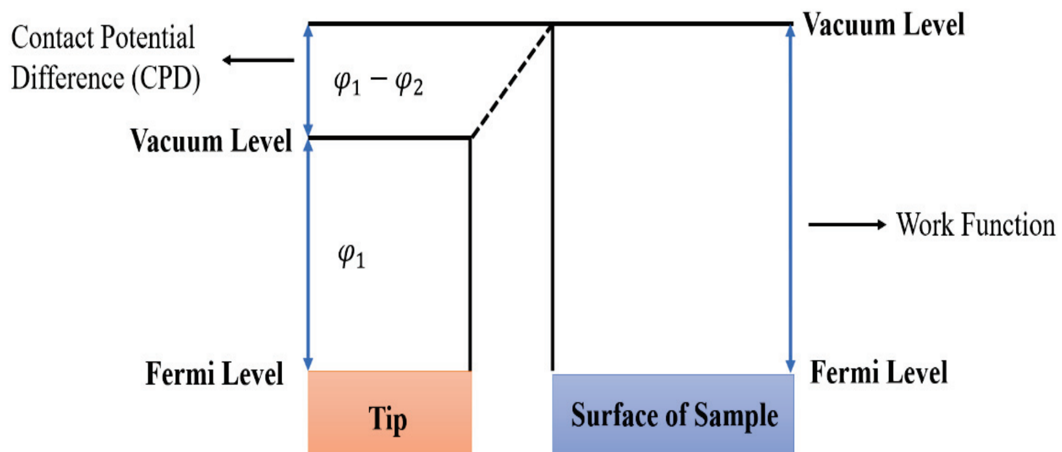

Figure 19. Band diagram of tip and sample in KPFM.

In the literature, there are many studies about the work function of functionalized graphene layers by measured KPFM [60,78] . The work function is related to the Fermi level of substrate, by comparison of the intact of graphene and doped graphene, shift in the Fermi level can be measured. This difference gives an idea about the carrier type after doping process [79,80]. In this thesis, KPFM is used to determine the work function of CVD grown graphene on n-type Si substrate. KPFM technique was performed using commercial Scanning Probe Microscopy (SPM) instrument (Solver Pro 7 from NT-MDT, Russia).

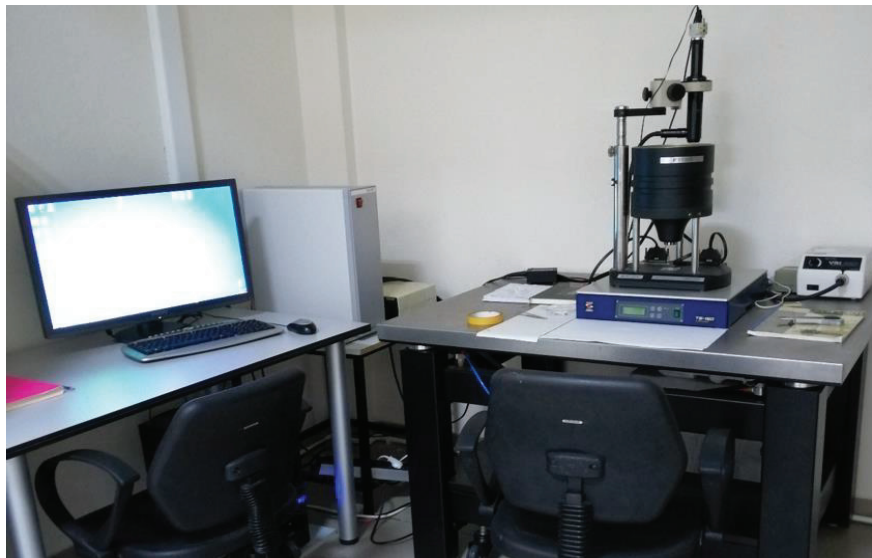

Figure 20. AFM setup in Quantum Device Laboratory, Physics Department at IZTECH.

2.4.4. Electronic and Optoelectronic Measurements Setup

Electronic and optoelectronic characterizations were performed by using the rack unit with necessary equipment including Keithley 2400 source-meter unit - Keithley 6220 Precision Current Source as voltage and current sources, Keithley 6485 Picoammeter - Keithley 2000 Digital Multimeter for precise current and voltage measurements and Pfeiffer High Cube TMP for high vacuum applications.

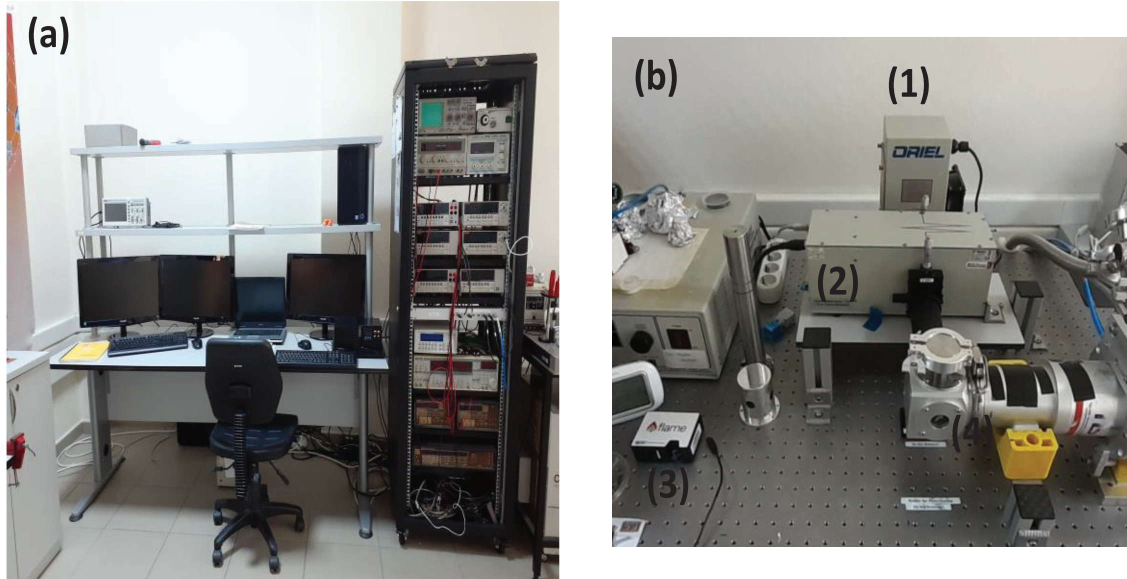

Figure 21. Laboratory at IZTECH. (b) The photocurrent spectroscopy setup; a quartz tungsten halogen lamp (Osram, 275 W) (1), a high resolution monochromator (Newport, Oriel Cornerstone) (2), flame spectrometry (Oceans Optics) (3). a closed loop cryostat (4).

2.4.4.1. Photocurrent Spectroscopy Setup

With the photocurrent spectroscopy setup illumination power dependent transient photocurrent and wavelength dependent photoresponsivity measurements of photodiode/photodetector devices can be done. The PS setup (see Figure 21(b)) is comprised of a quartz tungsten halogen lamp (Osram, 275 W) (1), a high resolution monochromator (Newport, Oriel Cornerstone) (2), flame spectrometry (Oceans Optics) (3). Also, the PS setup is integrated to a closed loop cryostat (5 K to 300 K) (see Figure 21(b) (4)) which enables temperature dependent measurements under a vacuum level of low 10^{-5} mbar. The entire setup is PC controlled and interfaced with GPIB card and connectors. The sample corded to the pins is placed to the sample holder of the cryostat which is electrically connected to the rack unit as shown in Figure 22.

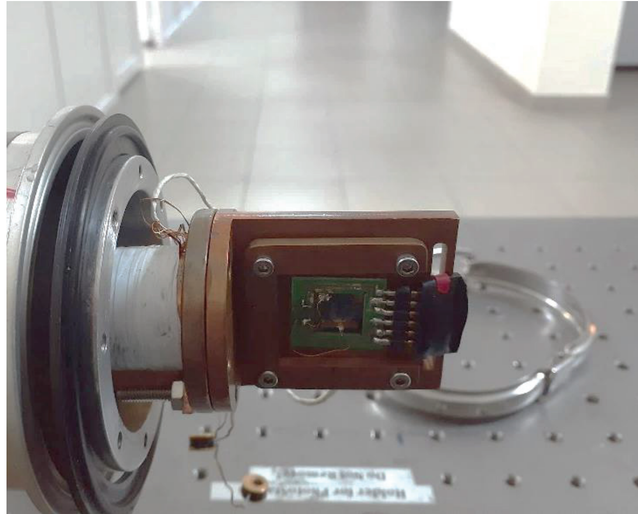

Figure 22. Picture of the sample after mounted onto the sample holder of cryostat.

To investigate the optoelectronic characteristics of Gr/Si photodiode, tungsten halogen lamp was used for light generation and specific wavelengths were separated by the help of a monochromator containing an internal shutter unit. Prior to the measurement, an optical spectrometer (Oceans Optics, Flame Spectrometry) was used for full-width half-maximum (FWHM) light calibration by tuning the spectrometer slit. Then, the illumination power on the device was measured by determining the power output of the calibration Si Photodiode FDS10X10 (Thorlabs). Time-resolved dark current and photocurrent measurements and wavelength dependent responsivity (A/W) measurements were conducted by using Keithley 2400 source-meter as the voltage source and Keithley 6485 Picoammeter to measure the dark current and photocurrent of the sample.

2.4.4.2. Probe Station

To determine both the mobility (μ) and sheet carrier density (n_s), it is necessary to perform Hall effect measurements. For the measurements, contacts must be deposited in the geometry of Van der Pauw configuration (containing four very small ohmic contacts

preferably placed at the corners of the sheet). The rectangular schematic with the Van der Pauw configuration is shown in Figure 23.

A probe station was used (which is named as “Black Box” in our laboratory (Figure 24 (b)) including the proper orientation of the pins for van der Pauw geometry. It has connection to Keithley 6220 Precision Current Source and Keithley 2000 Digital Multimeter which allow us to measure the sheet resistance and sheet carrier density of the thin films, additionally conduct 2-Terminal (2W) I-V measurements. A permanent neodymium magnet providing a magnetic field of 0.33 T was used for Hall Effect measurements.

In order to perform measurement of sheet carrier density and mobility of Gr/Si photodiode depending illumination power, the sample is illuminated with 850 nm led light (LED851L, Thorlabs). The illumination power on the device has been calibrated using Si photodiode with measuring power output by varying distance. Then the setup was prepared as seen in Figure 24, the distance between led and the device was arranged using z-stage. The measurements were conducted under dark condition.

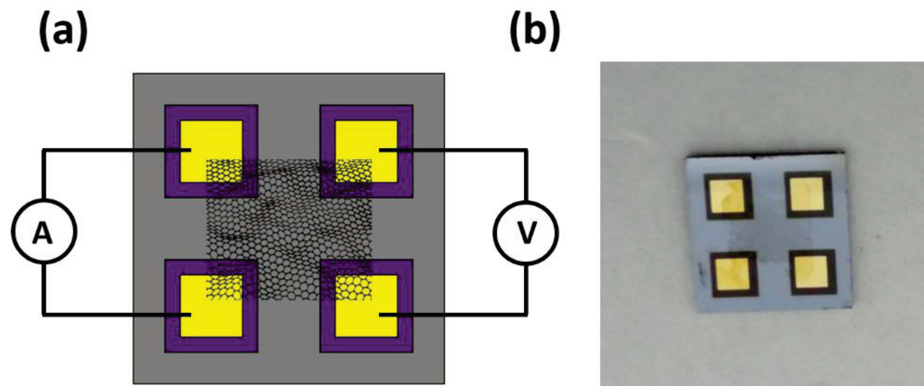

Figure 23. (a) Configuration for four probe Van der Pauw electrical conductivity measurement (graphene touches the contacts representatively). (b) Device configuration of four probe Cr/Au contacts on SiO_2 and graphene touching contacts on n-Si substrate.

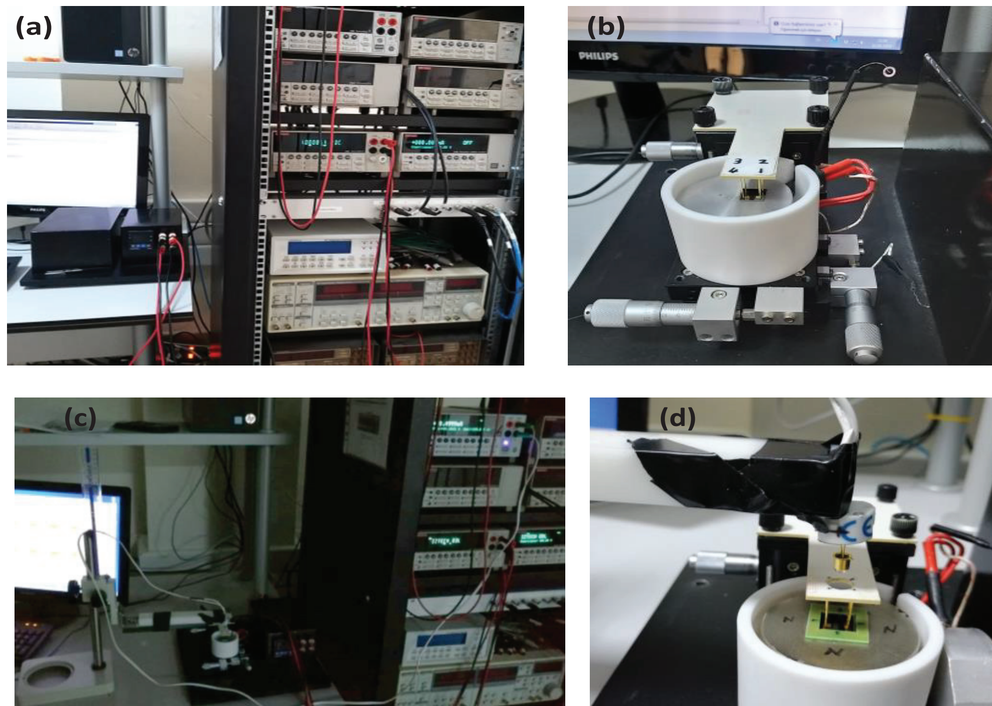

Figure 24. (a) The probe station setup. (b) The probes which are connected independently of each other and the holder has ability to move x,y and z directions. (c) The probe station setup with led integrated z- stage and (d) while led is on the device during Hall effect measurement.

CHAPTER 3

RESULTS AND DISCUSSION

3.1. Characterization of Gr/n-Si Schottky Diodes

3.1.1. Optical Microscope and Raman Spectroscopy Measurements

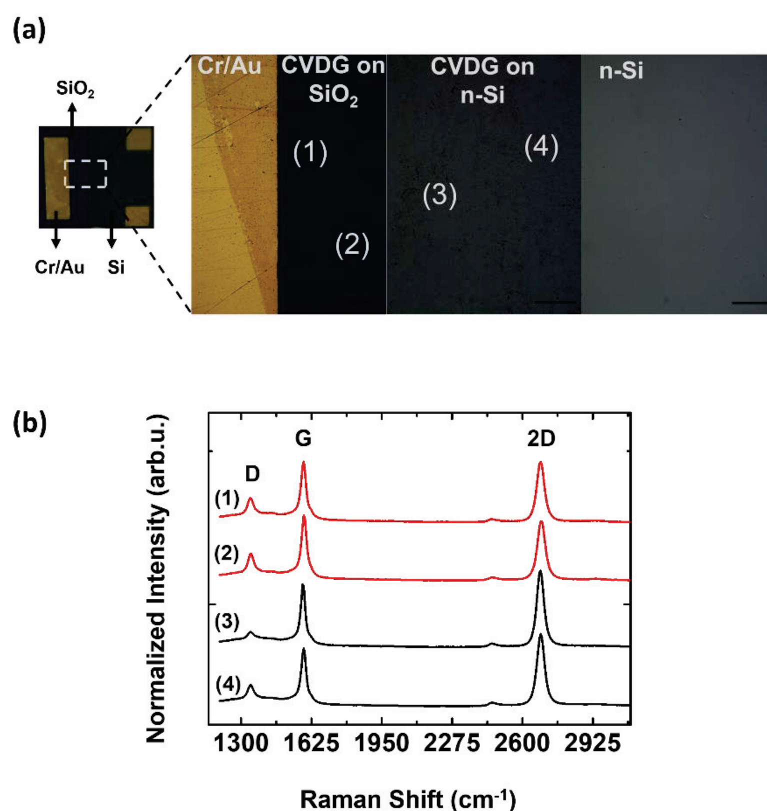

Figure 25. (a) The photograph of graphene/Si device and optical image collected different regions of the sample (scale bar is 40 μm) and (b) Raman spectra of CVD graphene (CVDG) collected from different regions of the sample.

Figure 25 (a) shows the optical microscopy image of Gr/n-Si device that was collected from different regions of the sample. Figure 25 (b) shows the randomly collected Raman spectra of CVD grown graphene (CVDG) where the graphene related peaks D (~ 1369 cm^{-1}), G (~1590 cm^{-1}), and 2D peaks (~2718 cm^{-1}) are resolved on SiO_2 and Si substrate. The strong G peak and the weak D peak indicate good graphitic quality, and the large 2D to G peak intensity ratio confirms the bilayer ($I_{2D}/I_G \sim 1$) [81,82] nature of CVDG. The obtained Raman spectrum reveals that the relatively small intensity of the defect band, both intensity ratios and narrow full width at half maximum of the 2D peak verify the existence of transferred high crystalline quality bilayer CVDG [83,84] even after the transfer process. The CVDG layer contains residues originating from the PR assisted transfer of CVDG from Cu foil onto both SiO_2 and Si substrate [85].

3.1.2. KPFM Analysis

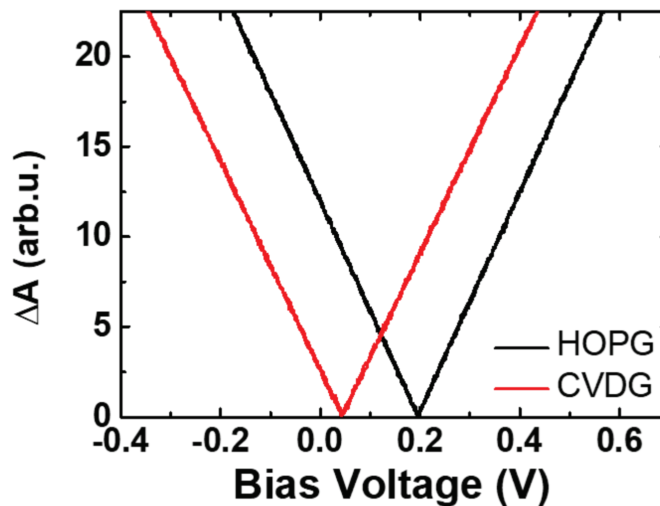

Figure 26. Contact potential differences of HOPG and CVDG on n-Si.

In order to determine the work function of bilayer CVDG under dark environment KPFM measurements were done using conductive AFM tip. Contact potential difference

(CPD) between the tip and sample (CPD = $\Phi_{TIP} - \Phi_{SAMPLE}$) was measured with this technique. Conductive TiN coated tip with thickness of 35 nm (NT-MDT, Russia) was used to obtain CPD signals and calibrated with HOPG (Φ_{HOPG} = 4.6 eV) as reference due to the constant work function in air and inert environment [86]. The work function of CVDG were determined as mentioned in Ref [[87]]. Figure 26 shows the cantilever oscillation amplitude (ΔA) versus bias voltage. When ΔA signal is close to zero due to feedback in the SPM system, interaction forces between tip and samples become zero and applied DC voltage to the tip becomes equal to CPD. With the KPFM measurements the work function of bilayer graphene on n-Si substrate was found as 4.45 eV.

$$\phi_B = \Phi_G - \chi \tag{3.1}$$

Where ϕ_B is the Schottky barrier height of graphene, Φ_G is the work function of graphene (Φ_G = 4.45 eV) and χ is electron affinity of graphene (χ = 4.5 eV) . From the Equation 3.1 ϕ_B was calculated as 0.4 eV.

3.1.3. Electrical Characterization of Gr/n-Si Schottky Diodes

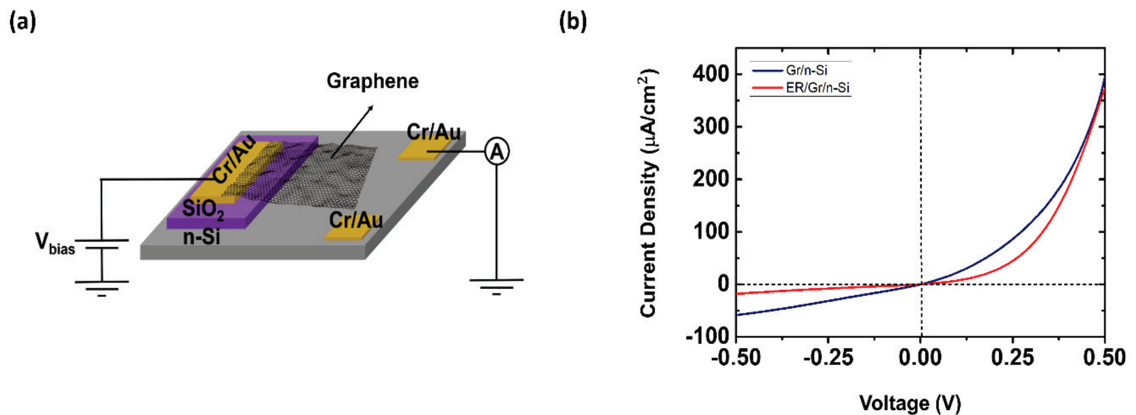

Figure 27. (a) Schematics of Gr/n-Si device structure and (b) J-V characteristics of Gr/n-Si and ER/Gr/n-Si devices under dark.

The I–V characteristics of Schottky diode are observed at semi-logarithmic scale and can be investigated by the thermionic emission [88]. When the Equation 1.6 is rearranged and differentiated with respect to I, the ideality factor (η) can be extracted by using the Equation 3.2 η can be determined from the intercept of dV/dln(I) vs. I plot which derives from forward bias of I-V curve of linear region. Additionally, in order to determine ϕ_B of the devices H(I) function is defined as the Equation 3.3.

$$\eta = \frac{q}{kT}\frac{dV}{d\ln(I)} \tag{3.2}$$

$$H(I) = V - \eta\frac{kT}{q}\ln\left(\frac{I}{AA^{*}T^{2}}\right) = IR_S + \eta(\phi_B) \tag{3.3}$$

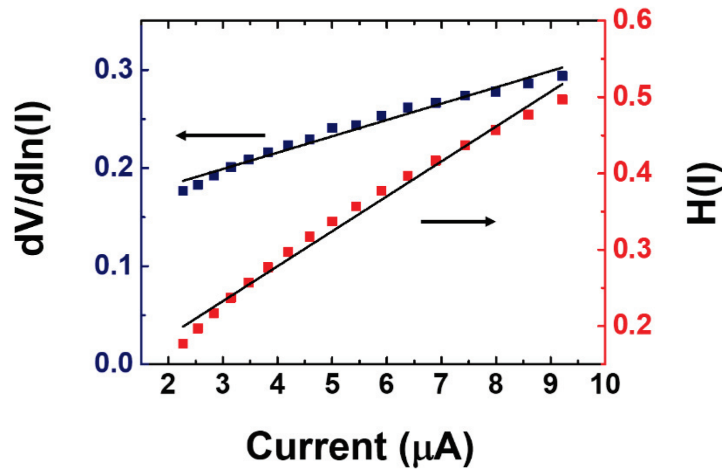

Figure 28. dV/dln (I) vs I and H(I) vs I plots of Gr/n-Si Schottky diode.

Plots of dV/dln(I) vs. I and H(I) vs. I for the Gr/n-Si diode were shown in Figure 28 and the electrical parameters were calculated using the plots. The η is calculated as 5.42. For an ideal diode η is equal to 1 but it generally has greater values. According to the literature the η values for graphene Schottky junctions are in the range ∼1.3− 30 which are far from ideal value [53,54,89]. Some recent studies have shown that the inhomogeneity at the graphene /semiconductor junction [4] is a cause of nonideality. This can lead to high

leakage currents and low values for η [5,89]. High values of η can be explained by the existence of the interfacial thin layer, inhomogeneities of ϕ_B distribution and the bias voltage dependence of ϕ_B [90].

The series resistance of the device (R_s) can be defined as the combination of contact resistance between graphene and Si, resistivity of graphene and Si and resistance of connecting wires [91]. From the slope of dV/dln(I) vs. I plot the R_s is calculated as 1664 Ω. Also, ϕ_B of the Gr/n-Si diode is calculated from Equation 3.3 as 0.48 eV. From the literature some n and ϕ_B of the Gr/n-Si diodes are listed in Table 2. From the literature, the results are similar to bilayer graphene/n-Si device type which also confirms with the Raman measurements of the CVD graphene.

Table 2. Ideality factor (η) and Schottky Barrier Height (ϕ_B) of the Gr/n-Si diodes.

Device Type	**Ideality factor (η)**	**Schottky Barrier Height (ϕ_B)**	**Reference**
Bilayer graphene/n-Si	4.89-7.69	0.41	[53]
Graphene/n-Si	1.2-5	0.86	[4]
Graphene/n-Si	2.53	0.83	[11]
Graphene/n-Si	1.6-2	0.79	[54]
Graphene/n-Si	5.42	0.48	This work

3.2. Electronic and Optoelectronic Characterization of Gr/n-Si Photodiodes

3.2.1. Electronic Characterization of Gr/n-Si Photodiodes

Figure 29 and Figure 30 show the J-V plots of the photodiodes in the dark and under illumination in the linear and semi-logarithmic scale. The dark current and the photocurrent were measured with voltage varies from -0.5 V to 0.5 V. The optoelectronic

characteristics of the Gr /n-Si photodiodes has been further investigated under 850 nm light with illumination power density (P_i) of 25 μW/cm^2. The light illumination gives rise to electron-hole pair generation at the depletion region of n-Si substrate beneath the graphene layer.

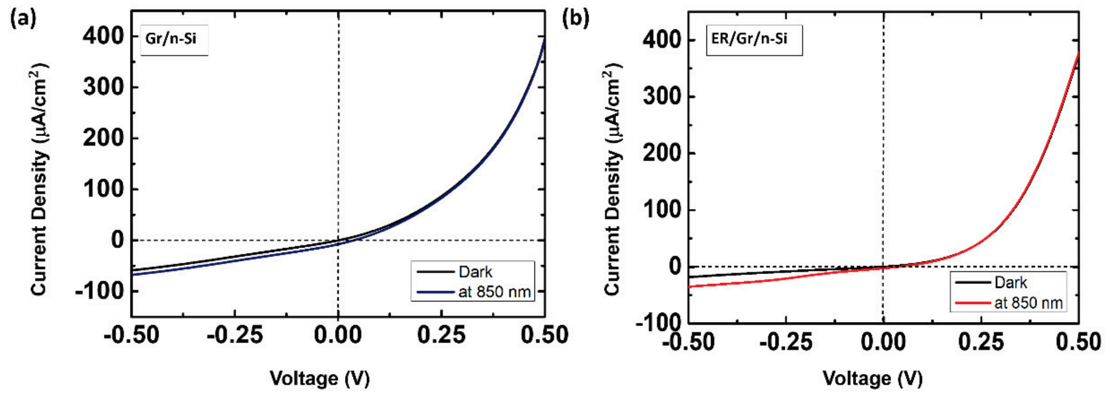

Figure 29. J-V characteristics of (a) Gr/n-Si and (b) ER/Gr/n-Si devices under dark and 850 nm light with illumination power density of 25 μW/cm^2.

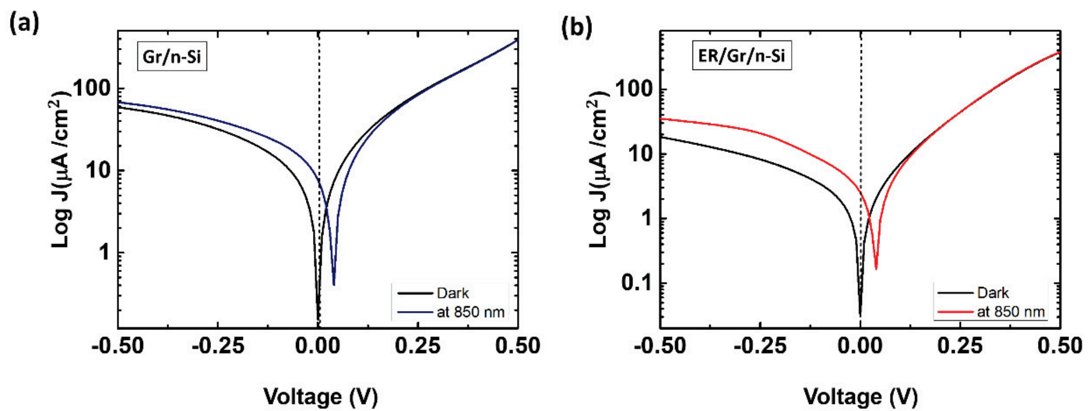

Figure 30. J-V characteristics of (a) Gr/n-Si and (b) ER/Gr/n-Si devices in semi-logaritmic scale under dark and 850 nm light with illumination power density of 25 μW/cm^2.

The holes are injected into the graphene from Si side and this leads to a measurable photocurrent for the Gr/n-Si device. The J-V measurements under dark and light illumination reveal the difference of dark and photocurrent of the devices. For Gr/n-Si and ER/Gr/n-Si devices the dark current densities are 150 nA/cm^2 and 30 nA/cm^2, respectively. The photocurrent (I_{sc}) densities are 7.7 μA/cm^2 and 2.5 μA/cm^2 for Gr/n-Si and ER/Gr/n-Si devices, respectively.

For both Gr/n-Si and ER/Gr/n-Si devices the open circuit voltage (V_{oc}) was measured as 40 mV. If the V_{oc} in the Schottky junction is low, the photogenerated carriers readily recombine themselves in the depletion region without contributing to the external photocurrent in the circuit. Such a small increase in the dark current is attributed to the presence of high-density surface states. At V=0 the dark current of the devices has the lowest values and the photo generated current approaches a saturation value at reverse bias region as seen in Figure 29. This infers that the built-in electric field is sufficiently strong enough to separate most of the generated e-h pairs. Therefore, the device can be operated at zero bias (self-powered) condition.

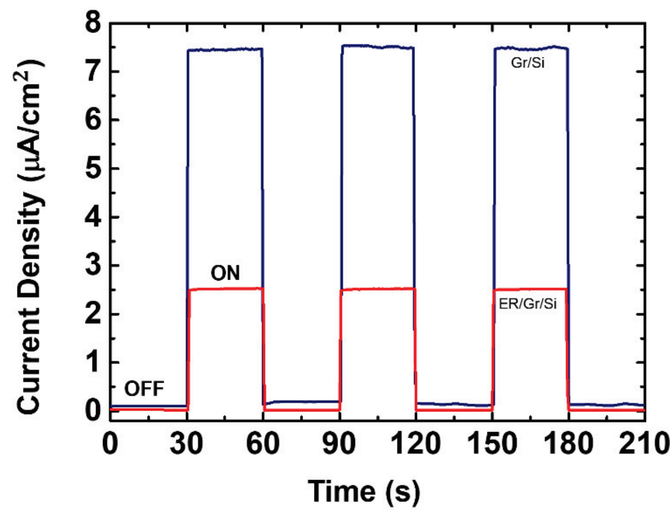

Figure 31. Photoswitching behavior of the Gr/n-Si and ER/Gr/n-Si photodiodes under 850 nm light with illumination power density of 25 μW/cm^2 at zero bias.

Time-dependent photocurrent measurements of Gr/n-Si and ER/Gr/n-Si photodiodes were done over several switching on/off cycles under 850 nm light illumination at zero bias. The measurements were performed at a total time of 210 s for

30 s intervals. As shown in Figure 31, the measured current of the devices display two different states at P_i of 25 μW/cm^2 ; a low-current density state at around 0.1 μA/cm^2 under dark and average photocurrents of about 7.4 μA/cm^2 and 2.5 μA/cm^2 for Gr/n-Si and ER/Gr/n-Si photodiodes, respectively. For both devices photoswitching characteristics have reversible behavior and good stability. However, encapsulated device has more stable and uniform profile.

Energy band diagram of Gr/n-Si junction under dark and light illumination are shown in Figure 36 (b). When the graphene layer is in contact with n-Si a depletion region and Schottky barrier (ϕ_b) were established at the Gr/n-Si interface owing to the difference between their Fermi levels [92,93]. This gives rise to efficient separation of the photogenerated carriers in the depletion region. While the holes move towards the graphene, the electrons are transferred in to the Si side, enhancing the photocurrent of the device.

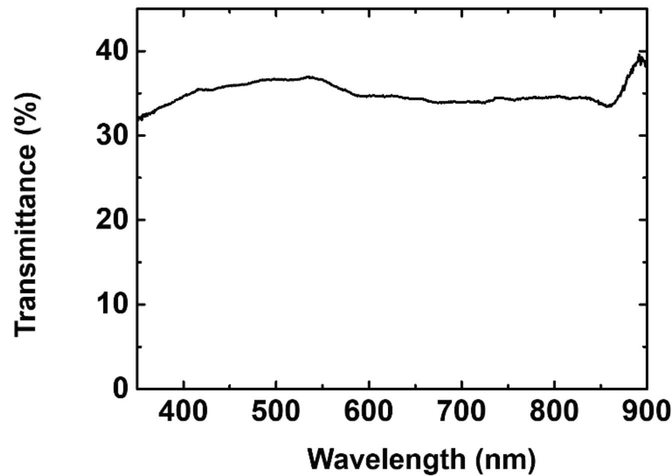

Figure 32. UV-Visible Spectrum of Epoxy Resin (ER).

The ability of the photodiode to convert the incoming light energy into electrical energy is called the external quantum efficiency (η) and is expressed as a percentage (%). Wavelength dependent η can be calculated by using Equation 3.4;

$$\eta = \frac{I_{ph}/e}{\frac{P_o\lambda}{hc}} \quad (3.4)$$

where, I_{ph} is the photocurrent at zero bias, P_o is the incident power, h is the Planck constant, e is the elementary charge, c is the speed of light and λ is the wavelength of incident light. Under 850 nm wavelength light illumination at zero bias, η of Gr/n-Si and ER/Gr/n-Si photodiodes were determined as 45 % and 14.6 % respectively. Due to the low optical transmission of ER, η of the encapsulated device decreases as shown in Figure 32. The wavelength dependent η of Gr/n-Si devices value are consistent with the results reported in the literature [54,94].

3.2.2. Photoresponsivity of Gr/n-Si Photodiodes

Photoresponsivity (R) is as one of the most important parameters for the light sensing capability of photodetector devices and can be expressed as [95] ;

$$R = (I_{photo} - I_{dark}) / P \quad (3.5)$$

where I_{photo} is the photocurrent, I_{dark} is the dark current and P is the optical power of incident light.

The obtained maximum responsivity of Gr/n-Si device reached about 0.56 AW^{-1} at the wavelength range of 750-850 nm, in correlation with typical optical absorption spectrum of n-type Si. However, the corresponding photoresponsivity showed a tendency to decrease below the cut-off wavelength of 1100 nm, which corresponds to an energy level that is below the band gap energy of Si. For ER/Gr/Si photodiode the obtained maximum responsivity is 0.1 AW^{-1} at the wavelength range of 750-850 nm. The responsivity value of Gr/n-Si as self powered photodiode is similar when compared to the reported literature [3,57,59].

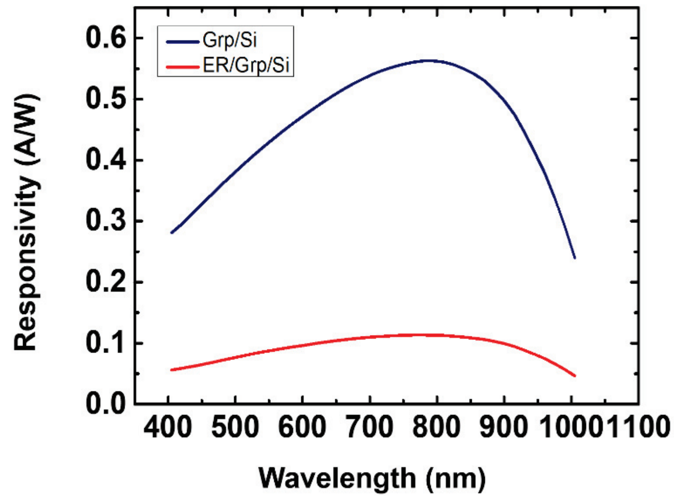

Figure 33. Responsivity of Gr/n-Si and ER/Gr/n-Si photodiodes at zero bias.

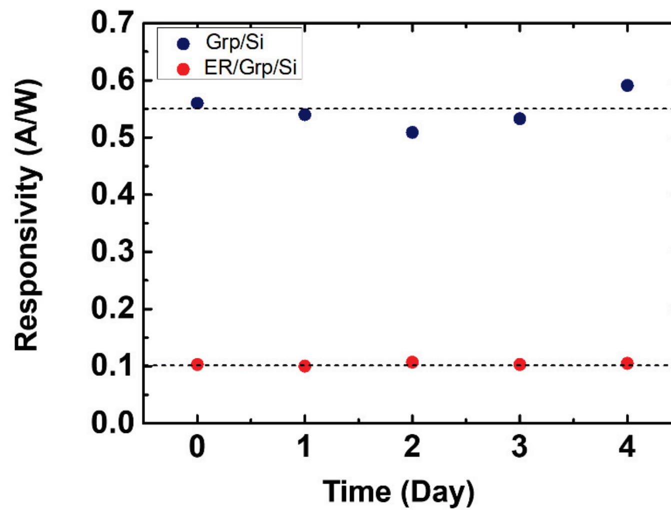

Figure 34. Time dependent responsivity measurements of Gr/n-Si and ER/Gr/n-Si photodiodes.

Figure 34 shows the responsivity values for Gr/n-Si and ER/Gr/n-Si photodiodes as a function of air-exposure time up to 5 days. Average deviation of responsivity values for Gr/n-Si and ER/Gr/n-Si photodiodes are 2.31 % and 0.18 %, respectively. Obviously, the average deviation values indicate that the responsivity becomes more stable by encapsulating the graphene. The adsorbates which caused by atmospheric gases affect the

electrical properties of graphene based devices [12]. Due to encapsulation the interaction of sample with adsorbates is suppressed.

3.3. Electrical Characteristics of Gr/n-Si Schottky Photodiode under Illumination with Various Power Density

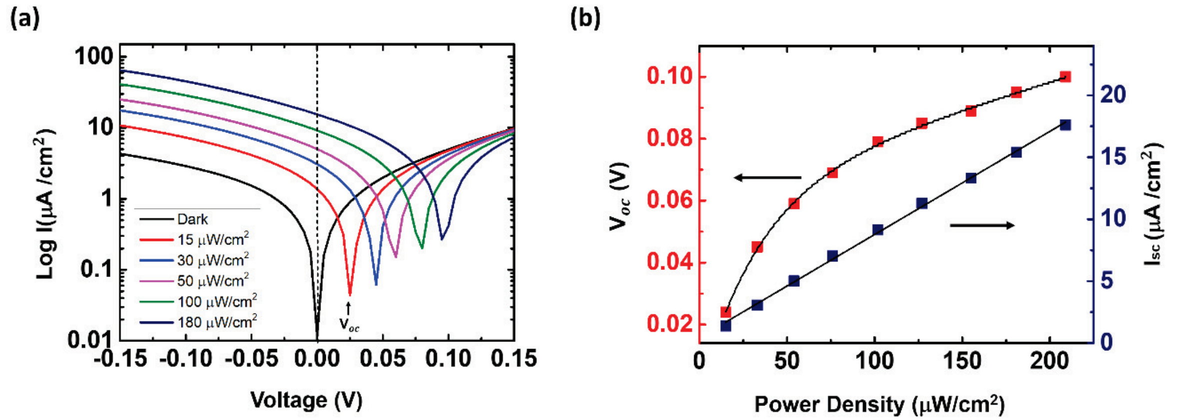

Figure 35. (a) I-V plot of the CVDG/n-Si device on a logarithmic scale in the dark and under illumination under various P_i of 15, 30, 50, 100 and 180 μW/cm², respectively and (b) The graph of P_i dependent V_{oc} and I_{sc} of the device (under self-powered conditions).

The I-V characteristics of Gr/n-Si device in semilogarithmic scale illuminated by 850 nm light with illumination power density (P_i) varying from 15 μW/cm² to 180 μW/cm² is shown in Figure 35 (a). With increasing P_i photogenerated carriers also increase which is proportional to the amount of absorbed photon flux. As seen in Figure 35 (b), while the P_i varied from 15 μW/cm² to 200 μW/cm², the short circuit current (I_{sc}) increased linearly from 0.14 μA to 1.76 μA at zero bias. This is indicating that a greater number of electron-hole pairs gets separated by the photoexcitation so the depletion width expands. As increasing P_i, the number of majority charge carriers (holes) in graphene also increase which causes the fermi level of graphene moves further below the dirac point. The linear increase in I_{sc} can be explained by the energy dispersion relation of graphene.

Due to linear increase in the density of states in valance band, photogenerated holes under illumination with increasing P_i also increases.

As shown in Figure 35 (b), V_{oc} increases from 0.02 V to 0.1 V as P_i increases from 15 $\mu W/cm^2$ to 200 $\mu W/cm^2$. The V_{oc} does not show linear response to P_i. When the plot of the V_{oc} vs. P_i is fitted with an exponential association function (Equation 3.6) there are fast and slow process which are characterized by the time constants t_1 and t_2.

$$y = A_o + A_1(1\text{-}\exp(\text{-}x/t_1)) + A_2(1\text{-}\exp(\text{-}x/t_2)) \qquad (3.6)$$

With the increment in electron-hole pairs which are created by the photoexcitation caused increase in hole concentration in graphene. Thus the fermi level of graphene moves further below its Dirac point which explains the fast increase of V_{oc}. Also, the increase in V_{oc} follows a decelerated trend and appears to be heading toward saturation with increasing P_i. As the increased P_i hole concentration in the depletion region increases and the holes have tendency to pass towards the graphene side, the photogenerated holes and the holes in the graphene will repulse each other due to Coulomb interaction. While the repulsion force between photogenerated holes and holes in graphene increases there occurs slow decrement in shifthing fermi level below the dirac point.

Due to the distinct work functions of graphene and Si, the electrons in Si lower their energy by flowing to graphene. This is because the fermi level of Si must equilibrate with the fermi level of graphene, leaving behind the positively charged states in the depletion region of the Si side. As a result, an upward bending of Si bands occurs to form a built-in electric field in the vicinity of the Gr/n–Si heterojunction interface. A cross-section of a diode under illumination and the specific band structure of the Gr/n–Si Schottky diode before (at thermal equilibrium) and after illumination is schematically shown in Figure 36 (a) and (b), respectively. Upon the light illumination, the holes in Si were transferred to the graphene layer resulting in lowering the Fermi level of graphene which led to a larger V_{oc} between n–Si and graphene. Difference between the fermi levels of graphene before and after illumination gives V_{oc} value as shown in Figure 36 (b). A larger V_{oc} gives rise to a wider depletion region providing an efficient dissociation of photogenerated carriers [60,96]. Higher V_{oc} leads to a higher ϕ_B of the Gr/n-Si junction.

Upon the light illumination lowering the Fermi level indicates increased hole concentration in the graphene. Hall Effect measurements showed that hole carrier concentration of graphene on n-Si substrate is increased with P_i. Under 850 nm

wavelength light illumination, P_i varying from 50 μW/cm^2 to 200 μW/cm^2 was used to measure the change in carrier density and mobility of graphene on n-Si substrate. Figure 37 presents the Hall measurement results with initial values of hole carrier concentration and mobility of Gr/n-Si device is 1.84 x 10^{13} cm^{-2} and 300.4 cm^2/V.s, respectively. With the increment of the P_i while the carrier concentration increases and the mobility decreases.

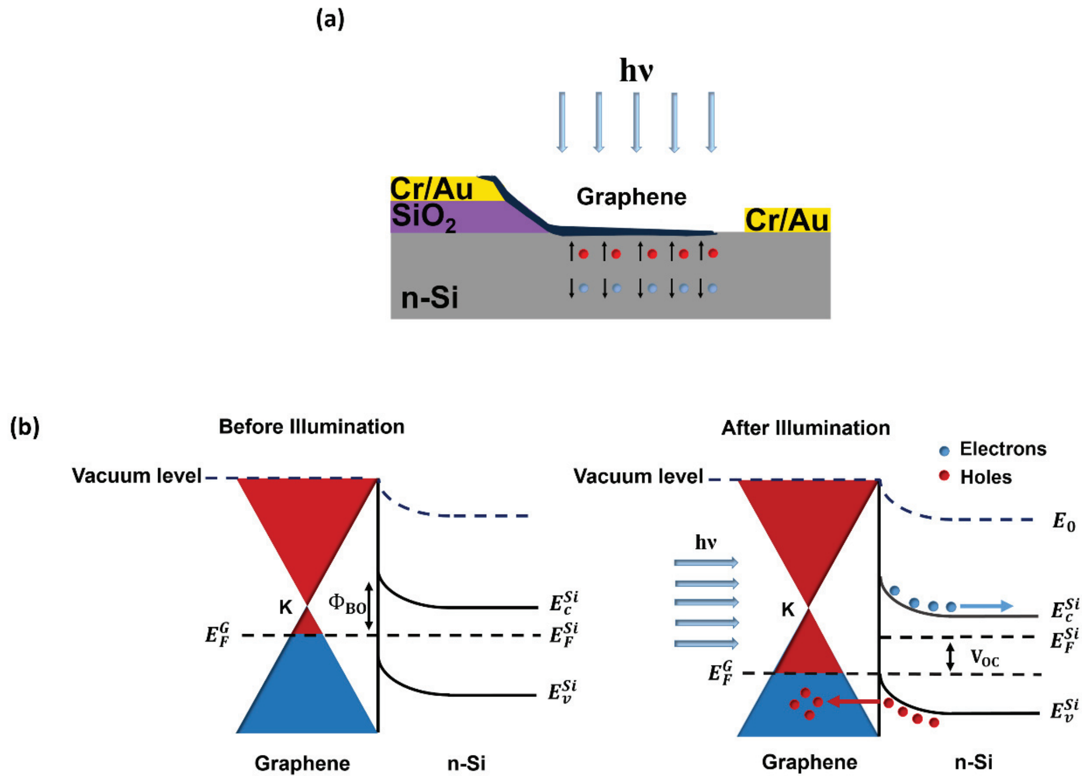

Figure 36. (a) Cross-section of Gr/n-Si heterojunction diode, (b) Schematic energy band diagram of the Gr/Si interface under dark and light illumination. The tunable V_{oc} with respect to the light illumination is clearly depicted and the red and blue arrow shows the direction of the movement of holes and electrons, respectively.

Additionally, assuming the electron affinity of Si (4.05 eV), we calculated the Schottky barrier height (ϕ_B) between graphene and n-Si as 0.4 eV (see Figure 38) before illumination. This relation is also identical with the theoretical prediction based on the

Schottky–Mott relation [97]. With increasing P_i we have seen that the value of the ϕ_B increases from 0.4 eV to 0.5 eV and has similar trend observed for V_{oc} vs. P_i.

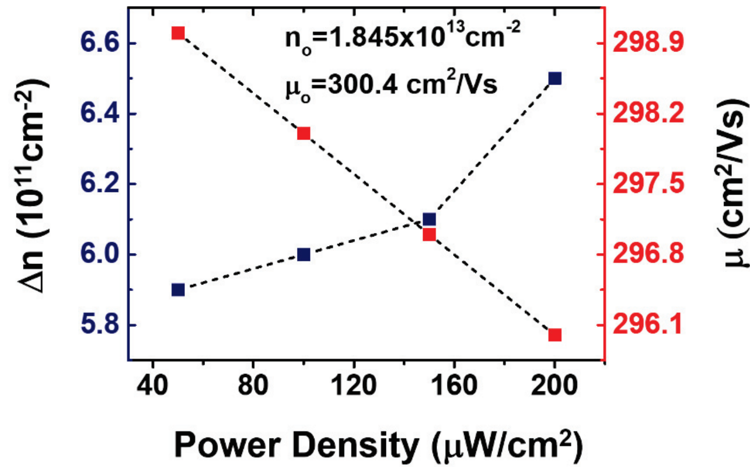

Figure 37. The graph of illumination power density dependent average carrier concentration and mobility of the Gr/n-Si device (at self-powered mode).

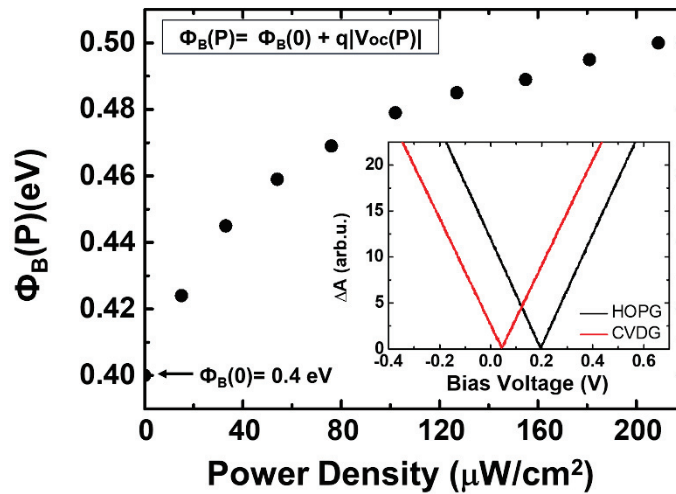

Figure 38. The graph of SBH (ϕ_B) differences with respect to different P_i values (inset shows the KPFM measurements of CVDG and HOPG. HOPG (black color) is used as reference).

CHAPTER 4

CONCLUSION

This thesis focused on the fabrication and characterization of CVD grown p-type graphene and n-Si (Gr/n-Si) forming Schottky junction photodiode which can operate at a wide spectral wavelength range between 390 and 1100 nm at photovoltaic (self-powered) mode.

In the first place, Gr/n-Si Schottky diode characteristics were investigated. The I-V characteristics of Gr /n-Si diode revealed Schottky barrier with rectifying behavior. The calculated value of Schottky barrier height is 0.48 eV and the measured Schottky barrier height value by KPFM method is 0.40 eV. Also, Gr/n-Si Schottky photodiode was encapsulated with Epoxy Resin (ER) to prevent graphene from atmospheric adsorbates. The electronic and optoelectronic characterizations of Gr/n-Si photodiodes were done before and after coating the devices with ER. Due to encapsulation the maximum obtained photoresponsivity value of the device was decreased from 0.56 AW^{-1} to 0.1 AW^{-1}. And external quantum efficiency of the devices were calculated as 45 % and 14.6 % for Gr/n-Si and ER/Gr/n-Si photodiodes, respectively. Moreover, the stability of the devices were investigated in terms of photoresponsivity. Average deviation of photoresponsivity values for Gr/n-Si and ER/Gr/n-Si photodiodes were found as 2.31 % and 0.18 %, respectively. Obviously, the obtained average deviation values indicated that the responsivity values were more stable by encapsulating the graphene. Also, time-resolved photocurrent spectroscopy measurements showed that the devices exhibited enhanced photodetector performance in terms of photo-switching characteristics and spectral responsivity.

Additionally, electrical characteristics of Gr/n-Si Schottky photodiode under illumination with various power density were investigated. We observed that with different illumination power densities (P_i), the short circuit current (I_{sc}) increased linearly from 0.14 μA to 1.76 μA at zero bias. However, open circuit voltage (V_{oc}) exhibited two phased slow and fast increment with increased P_i. The change in V_{oc} showed the shifting in fermi level of graphene. Hall effect measurements were conducted in order to

investigate the hole carrier concentration and mobility of the graphene on n-Si. We observed that with the increment of the P_i the carrier concentration increased and the mobility decreased. Therefore, we proved that with increased P_i hole concentration of graphene increased and fermi level of Gr/n-Si heterojunction shifted downwards. Besides, light induced manipulation of the Schottky barrier height of Gr/n-Si photodiode was studied. With increasing P_i we found that Schottky barrier height of the device increased from 0.4 eV to 0.5 eV and showed similar trend as in V_{oc}.

REFERENCES

(1) Novoselov, K. S.; Geim, A. K.; Morozov, S. V.; Jiang, D.; Katsnelson, M. I.; Grigorieva, I. V.; Dubonos, S. V.; Firsov, A. A. Two-Dimensional Gas of Massless Dirac Fermions in Graphene. *Nature* 2005. https://doi.org/10.1038/nature04233.

(2) Geim, A. K.; Novoselov, K. S. The Rise of Graphene. *Nat. Mater.* 2007, *6*, 183.

(3) Periyanagounder, D.; Gnanasekar, P.; Varadhan, P.; He, J. H.; Kulandaivel, J. High Performance, Self-Powered Photodetectors Based on a Graphene/Silicon Schottky Junction Diode. *J. Mater. Chem. C* 2018. https://doi.org/10.1039/c8tc02786b.

(4) Tongay, S.; Lemaitre, M.; Miao, X.; Gila, B.; Appleton, B. R.; Hebard, A. F. Rectification at Graphene-Semiconductor Interfaces: Zero-Gap Semiconductor-Based Diodes. *Phys. Rev. X* 2012. https://doi.org/10.1103/PhysRevX.2.011002.

(5) Tongay, S.; Schumann, T.; Hebard, A. F. Graphite Based Schottky Diodes Formed on Si, GaAs, and 4H-SiC Substrates. *Appl. Phys. Lett.* 2009. https://doi.org/10.1063/1.3268788.

(6) Tongay, S.; Schumann, T.; Miao, X.; Appleton, B. R.; Hebard, A. F. Tuning Schottky Diodes at the Many-Layer-Graphene/Semiconductor Interface by Doping. *Carbon N. Y.* 2011. https://doi.org/10.1016/j.carbon.2011.01.029.

(7) Kim, H. Y.; Lee, K.; McEvoy, N.; Yim, C.; Duesberg, G. S. Chemically Modulated Graphene Diodes. *Nano Lett.* 2013. https://doi.org/10.1021/nl400674k.

(8) Garg, R.; Dutta, N.; Choudhury, N. Work Function Engineering of Graphene. *Nanomaterials* 2014. https://doi.org/10.3390/nano4020267.

(9) Jo, G.; Na, S. I.; Oh, S. H.; Lee, S.; Kim, T. S.; Wang, G.; Choe, M.; Park, W.; Yoon, J.; Kim, D. Y.; et al. Tuning of a Graphene-Electrode Work Function to Enhance the Efficiency of Organic Bulk Heterojunction Photovoltaic Cells with an Inverted Structure. *Appl. Phys. Lett.* 2010. https://doi.org/10.1063/1.3514551.

(10) Zhou, Y.; Fuentes-Hernandez, C.; Shim, J.; Meyer, J.; Giordano, A. J.; Li, H.; Winget, P.; Papadopoulos, T.; Cheun, H.; Kim, J.; et al. A Universal Method to Produce Low-Work Function Electrodes for Organic Electronics. *Science (80-.).* 2012. https://doi.org/10.1126/science.1218829.

(11) Parui, S.; Ruiter, R.; Zomer, P. J.; Wojtaszek, M.; Van Wees, B. J.; Banerjee, T. Temperature Dependent Transport Characteristics of Graphene/n-Si Diodes. *J. Appl. Phys.* 2014. https://doi.org/10.1063/1.4905110.

(12) Kalkan, S. B.; Aydln, H.; Özkendir, D.; Çelebi, C. The Effect of Adsorbates on the Electrical Stability of Graphene Studied by Transient Photocurrent Spectroscopy. *Appl. Phys. Lett.* 2018. https://doi.org/10.1063/1.5011454.

(13) Yuan, H.; Chang, S.; Bargatin, I.; Wang, N. C.; Riley, D. C.; Wang, H.; Schwede, J. W.; Provine, J.; Pop, E.; Shen, Z. X.; et al. Engineering Ultra-Low Work Function of Graphene. *Nano Lett.* 2015. https://doi.org/10.1021/acs.nanolett.5b01916.

(14) Castro Neto, A. H.; Guinea, F.; Peres, N. M. R.; Novoselov, K. S.; Geim, A. K. The Electronic Properties of Graphene. *Rev. Mod. Phys.* 2009. https://doi.org/10.1103/RevModPhys.81.109.

(15) Giubileo, F.; Di Bartolomeo, A. The Role of Contact Resistance in Graphene Field-Effect Devices. *Progress in Surface Science*. 2017. https://doi.org/10.1016/j.progsurf.2017.05.002.

(16) A.K. Geim and K.S. Novoselov. The Rise of Graphene PROGRESS. *Nat. Mater.* 2007. https://doi.org/10.1038/nmat1849.

(17) Zhang, Y.; Tan, Y. W.; Stormer, H. L.; Kim, P. Experimental Observation of the Quantum Hall Effect and Berry's Phase in Graphene. *Nature* 2005. https://doi.org/10.1038/nature04235.

(18) Katsnelson, M. I.; Novoselov, K. S.; Geim, A. K. Chiral Tunnelling and the Klein Paradox in Graphene. *Nat. Phys.* 2006. https://doi.org/10.1038/nphys384.

(19) Cheianov, V. V.; Fal'ko, V.; Altshuler, B. L. The Focusing of Electron Flow and

a Veselago Lens in Graphene P-n Junctions. *Science (80-.).* 2007. https://doi.org/10.1126/science.1138020.

(20) Geim, A. K.; Novoselov, K. S. The Rise of Graphene. In *Nanoscience and Technology: A Collection of Reviews from Nature Journals*; 2009. https://doi.org/10.1142/9789814287005_0002.

(21) Balandin, A. A.; Ghosh, S.; Bao, W.; Calizo, I.; Teweldebrhan, D.; Miao, F.; Lau, C. N. Superior Thermal Conductivity of Single-Layer Graphene. *Nano Lett.* 2008. https://doi.org/10.1021/nl0731872.

(22) Lee, C.; Wei, X.; Kysar, J. W.; Hone, J. Measurement of the Elastic Properties and Intrinsic Strength of Monolayer Graphene. *Science (80-.).* 2008. https://doi.org/10.1126/science.1157996.

(23) Han, J. T.; Jeong, S. Y.; Jeong, H. J.; Lee, G.-W. Chemically Exfoliated Graphene Nanosheets for Flexible Electrode Applications. In *Graphene Oxide - Applications and Opportunities*; 2018. https://doi.org/10.5772/intechopen.77284.

(24) Yoo, E. J.; Kim, J.; Hosono, E.; Zhou, H. S.; Kudo, T.; Honma, I. Large Reversible Li Storage of Graphene Nanosheet Families for Use in Rechargeable Lithium Ion Batteries. *Nano Lett.* 2008. https://doi.org/10.1021/nl800957b.

(25) Stoller, M. D.; Park, S.; Yanwu, Z.; An, J.; Ruoff, R. S. Graphene-Based Ultracapacitors. *Nano Lett.* 2008. https://doi.org/10.1021/nl802558y.

(26) AK, G. Graphene: Status and Prospects. *Science (80-.).* 2009.

(27) Kim, K. S.; Zhao, Y.; Jang, H.; Lee, S. Y.; Kim, J. M.; Kim, K. S.; Ahn, J. H.; Kim, P.; Choi, J. Y.; Hong, B. H. Large-Scale Pattern Growth of Graphene Films for Stretchable Transparent Electrodes. *Nature* 2009. https://doi.org/10.1038/nature07719.

(28) Li, X.; Cai, W.; An, J.; Kim, S.; Nah, J.; Yang, D.; Piner, R.; Velamakanni, A.; Jung, I.; Tutuc, E.; et al. Large-Area Synthesis of High-Quality and Uniform Graphene Films on Copper Foils. *Science (80-.).* 2009. https://doi.org/10.1126/science.1171245.

(29) Suk, J. W.; Lee, W. H.; Lee, J.; Chou, H.; Piner, R. D.; Hao, Y.; Akinwande, D.; Ruoff, R. S. Enhancement of the Electrical Properties of Graphene Grown by Chemical Vapor Deposition via Controlling the Effects of Polymer Residue. *Nano Lett.* 2013. https://doi.org/10.1021/nl304420b.

(30) Chan, J.; Venugopal, A.; Pirkle, A.; McDonnell, S.; Hinojos, D.; Magnuson, C. W.; Ruoff, R. S.; Colombo, L.; Wallace, R. M.; Vogel, E. M. Reducing Extrinsic Performance-Limiting Factors in Graphene Grown by Chemical Vapor Deposition. *ACS Nano* 2012. https://doi.org/10.1021/nn300107f.

(31) Sidorov, A. N.; Gaskill, K.; Buongiorno Nardelli, M.; Tedesco, J. L.; Myers-Ward, R. L.; Eddy, C. R.; Jayasekera, T.; Kim, K. W.; Jayasingha, R.; Sherehiy, A.; et al. Charge Transfer Equilibria in Ambient-Exposed Epitaxial Graphene on (0001̄) 6 H-SiC. In *Journal of Applied Physics*; 2012. https://doi.org/10.1063/1.4725413.

(32) Eriksson, J.; Pearce, R.; Iakimov, T.; Virojanadara, C.; Gogova, D.; Andersson, M.; Syväjärvi, M.; Lloyd Spetz, A.; Yakimova, R. The Influence of Substrate Morphology on Thickness Uniformity and Unintentional Doping of Epitaxial Graphene on SiC. *Appl. Phys. Lett.* 2012. https://doi.org/10.1063/1.4729556.

(33) Lartsev, A.; Yager, T.; Bergsten, T.; Tzalenchuk, A.; Janssen, T. J. B. M.; Yakimova, R.; Lara-Avila, S.; Kubatkin, S. Tuning Carrier Density across Dirac Point in Epitaxial Graphene on SiC by Corona Discharge. *Appl. Phys. Lett.* 2014. https://doi.org/10.1063/1.4892922.

(34) Morozov, S. V.; Novoselov, K. S.; Katsnelson, M. I.; Schedin, F.; Elias, D. C.; Jaszczak, J. A.; Geim, A. K. Giant Intrinsic Carrier Mobilities in Graphene and Its Bilayer. *Phys. Rev. Lett.* 2008. https://doi.org/10.1103/PhysRevLett.100.016602.

(35) Chen, J. H.; Jang, C.; Xiao, S.; Ishigami, M.; Fuhrer, M. S. Intrinsic and Extrinsic Performance Limits of Graphene Devices on SiO 2. *Nat. Nanotechnol.* 2008. https://doi.org/10.1038/nnano.2008.58.

(36) Mayorov, A. S.; Gorbachev, R. V.; Morozov, S. V.; Britnell, L.; Jalil, R.; Ponomarenko, L. A.; Blake, P.; Novoselov, K. S.; Watanabe, K.; Taniguchi, T.;

et al. Micrometer-Scale Ballistic Transport in Encapsulated Graphene at Room Temperature. *Nano Lett.* 2011. https://doi.org/10.1021/nl200758b.

(37) Li, X.; Magnuson, C. W.; Venugopal, A.; An, J.; Suk, J. W.; Han, B.; Borysiak, M.; Cai, W.; Velamakanni, A.; Zhu, Y.; et al. Graphene Films with Large Domain Size by a Two-Step Chemical Vapor Deposition Process. *Nano Lett.* 2010. https://doi.org/10.1021/nl101629g.

(38) Hao, Y.; Bharathi, M. S.; Wang, L.; Liu, Y.; Chen, H.; Nie, S.; Wang, X.; Chou, H.; Tan, C.; Fallahazad, B.; et al. The Role of Surface Oxygen in the Growth of Large Single-Crystal Graphene on Copper. *Science (80-.).* 2013. https://doi.org/10.1126/science.1243879.

(39) Luo, Z.; Pinto, N. J.; Davila, Y.; Charlie Johnson, A. T. Controlled Doping of Graphene Using Ultraviolet Irradiation. *Appl. Phys. Lett.* 2012. https://doi.org/10.1063/1.4729828.

(40) Fates, R.; Bouridah, H.; Raskin, J. P. Probing Carrier Concentration in Gated Single, Bi- and Tri-Layer CVD Graphene Using Raman Spectroscopy. *Carbon N. Y.* 2019. https://doi.org/10.1016/j.carbon.2019.04.078.

(41) Zhong, B.; Uddin, M. A.; Singh, A.; Webb, R.; Koley, G. Temperature Dependent Carrier Mobility in Graphene: Effect of Pd Nanoparticle Functionalization and Hydrogenation. *Appl. Phys. Lett.* 2016. https://doi.org/10.1063/1.4942975.

(42) Limbu, T. B.; Mendoza, F.; Barrionuevo, D.; Carpena, J.; Maruyama, B.; Katiyar, R. S.; Weiner, B. R.; Morell, G. Study on the Optical and Electrical Properties of Tetracyanoethylene Doped Bilayer Graphene Stack for Transparent Conducting Electrodes. *AIP Adv.* 2016. https://doi.org/10.1063/1.4945345.

(43) Nair, R. R.; Blake, P.; Grigorenko, A. N.; Novoselov, K. S.; Booth, T. J.; Stauber, T.; Peres, N. M. R.; Geim, A. K. Fine Structure Constant Defines Visual Transparency of Graphene. *Science (80-.).* 2008. https://doi.org/10.1126/science.1156965.

(44) Bonaccorso, F.; Sun, Z.; Hasan, T.; Ferrari, A. C. Graphene Photonics and

Optoelectronics. *Nat. Photonics* 2010, *4*, 611.

(45) Rhoderick, E. H. The Physics of Schottky Barriers. *Journal of Physics D: Applied Physics*. 1970. https://doi.org/10.1088/0022-3727/3/8/203.

(46) Pepper, M. Metal-Semiconductor Contacts. *Phys. Technol.* 1974. https://doi.org/10.1088/0305-4624/5/4/405.

(47) Henisch, H. K. Rectifying Semiconductor Contacts. *J. Electrochem. Soc.* 1957. https://doi.org/10.1149/1.2428607.

(48) Bardeen, J. Surface States and Rectification at a Metal Semi-Conductor Contact. *Phys. Rev.* 1947. https://doi.org/10.1103/PhysRev.71.717.

(49) H.A. Bethe. *MIT Radiation Laboratory Report, 43-12*.

(50) E. H. Rhoderick and R. H. Williams. *"Metal-Semiconductor Contacts," 2nd Edition,* 2nd editio.; Clarendon Press: Oxford, 1988.

(51) Reina, A.; Son, H.; Jiao, L.; Fan, B.; Dresselhaus, M. S.; Liu, Z. F.; Kong, J. Transferring and Identification of Single- and Few-Layer Graphene on Arbitrary Substrates. *J. Phys. Chem. C* 2008. https://doi.org/10.1021/jp807380s.

(52) Li, X.; Zhu, M.; Du, M.; Lv, Z.; Zhang, L.; Li, Y.; Yang, Y.; Yang, T.; Li, X.; Wang, K.; et al. High Detectivity Graphene-Silicon Heterojunction Photodetector. *Small* 2016. https://doi.org/10.1002/smll.201502336.

(53) Chen, C. C.; Aykol, M.; Chang, C. C.; Levi, A. F. J.; Cronin, S. B. Graphene-Silicon Schottky Diodes. *Nano Lett.* 2011. https://doi.org/10.1021/nl104364c.

(54) Miao, X.; Tongay, S.; Petterson, M. K.; Berke, K.; Rinzler, A. G.; Appleton, B. R.; Hebard, A. F. High Efficiency Graphene Solar Cells by Chemical Doping. *Nano Lett.* 2012. https://doi.org/10.1021/nl204414u.

(55) Zhang, Q.; Tang, L.; Luo, J.; Zhang, J.; Wang, X.; Li, D.; Yao, Y.; Zhang, Z. Direct Growth of Nanocrystalline Graphene/Graphite All Carbon Transparent Electrode for Graphene Glass and Photodetectors. *Carbon N. Y.* 2017. https://doi.org/10.1016/j.carbon.2016.09.060.

(56) Li, X.; Zhu, H.; Wang, K.; Cao, A.; Wei, J.; Li, C.; Jia, Y.; Li, Z.; Li, X.; Wu, D. Graphene-on-Silicon Schottky Junction Solar Cells. *Adv. Mater.* 2010. https://doi.org/10.1002/adma.200904383.

(57) An, X.; Liu, F.; Jung, Y. J.; Kar, S. Tunable Graphene-Silicon Heterojunctions for Ultrasensitive Photodetection. *Nano Lett.* 2013. https://doi.org/10.1021/nl303682j.

(58) Huang, K.; Yu, X.; Cong, J.; Yang, D. Progress of Graphene–Silicon Heterojunction Photovoltaic Devices. *Advanced Materials Interfaces*. 2018. https://doi.org/10.1002/admi.201801520.

(59) Wan, X.; Xu, Y.; Guo, H.; Shehzad, K.; Ali, A.; Liu, Y.; Yang, J.; Dai, D.; Lin, C.-T.; Liu, L.; et al. A Self-Powered High-Performance Graphene/Silicon Ultraviolet Photodetector with Ultra-Shallow Junction: Breaking the Limit of Silicon? *npj 2D Mater. Appl.* 2017, *1* (1), 4. https://doi.org/10.1038/s41699-017-0008-4.

(60) Sze, S. M.; Ng, K. K. *Physics of Semiconductor Devices: Third Edition*; 2006. https://doi.org/10.1002/9780470068328.

(61) Wang, X.-J.; Zou, L.; Li, D.; Zhang, Q.; Wang, F.; Zhang, Z. Photo-Induced Doping in Graphene/Silicon Heterostructures. *J. Phys. Chem. C* 2015, *119* (2), 1061–1066. https://doi.org/10.1021/jp509878m.

(62) Ravi, S. K.; Sun, W.; Nandakumar, D. K.; Zhang, Y.; Tan, S. C. Optical Manipulation of Work Function Contrasts on Metal Thin Films. *Sci. Adv.* 2018. https://doi.org/10.1126/sciadv.aao6050.

(63) Viktorovitch, P.; Kamarinos, G. Improvement of the Photovoltaic Efficiency of a Metal-Insulator- Semiconductor Structure: Influence of Interface States. *J. Appl. Phys.* 1977. https://doi.org/10.1063/1.324074.

(64) Ng, K. K.; Card, H. C. Photocurrent Suppression and Interface State Recombination in MIS-Schottky Barriers; 2008. https://doi.org/10.1109/iedm.1977.189161.

(65) Lillington, D. R.; Townsend, W. G. Effects of Interfacial Oxide Layers on the Performance of Silicon Schottky-Barrier Solar Cells. *Appl. Phys. Lett.* 1976. https://doi.org/10.1063/1.88654.

(66) Kermaninejad, H.; Najafi, F.; Soleimani-Gorgani, A. Encapsulation of Flexible Organic Light Emitting Diodes by UV-Cure Epoxy Siloxane. *J. Appl. Polym. Sci.* 2019. https://doi.org/10.1002/app.48033.

(67) Ho, T. H.; Wang, C. S. Modification of Epoxy Resin with Siloxane Containing Phenol Aralkyl Epoxy Resin for Electronic Encapsulation Application. *Eur. Polym. J.* 2001. https://doi.org/10.1016/S0014-3057(00)00115-4.

(68) Muñoz, R.; Gómez-Aleixandre, C. Review of CVD Synthesis of Graphene. *Chemical Vapor Deposition*. 2013. https://doi.org/10.1002/cvde.201300051.

(69) Shelton, J. C.; Patil, H. R.; Blakely, J. M. Equilibrium Segregation of Carbon to a Nickel (111) Surface: A Surface Phase Transition. *Surf. Sci.* 1974. https://doi.org/10.1016/0039-6028(74)90272-6.

(70) Ueta, H.; Saida, M.; Nakai, C.; Yamada, Y.; Sasaki, M.; Yamamoto, S. Highly Oriented Monolayer Graphite Formation on Pt(1 1 1) by a Supersonic Methane Beam. *Surf. Sci.* 2004. https://doi.org/10.1016/j.susc.2004.04.039.

(71) Gall, N. R.; Rut'kov, E. V.; Tontegode, A. Y. Interaction of Silver Atoms with Iridium and with a Two-Dimensional Graphite Film on Iridium: Adsorption, Desorption, and Dissolution. *Phys. Solid State* 2004. https://doi.org/10.1134/1.1649439.

(72) Blake, P.; Hill, E. W.; Castro Neto, A. H.; Novoselov, K. S.; Jiang, D.; Yang, R.; Booth, T. J.; Geim, A. K. Making Graphene Visible. *Appl. Phys. Lett.* 2007. https://doi.org/10.1063/1.2768624.

(73) Warner, J. H.; Schaffel, F.; Rummeli, M.; Bachmatiuk, A.; Schäffel, F.; Bachmatiuk, A.; Rümmeli, M. H. Graphene Fundamentals and Emergent Applications. *Graphene*. 2013. https://doi.org/10.1016/B978-0-12-394593-8.00001-1.

(74) Sur, U. K.; Chowdhury, J. Surface-Enhanced Raman Scattering: Overview of a Versatile Technique Used in Electrochemistry and Nanoscience. *Current Science*. 2013.

(75) Gao, L.; Ren, W.; Zhao, J.; Ma, L. P.; Chen, Z.; Cheng, H. M. Efficient Growth of High-Quality Graphene Films on Cu Foils by Ambient Pressure Chemical Vapor Deposition. *Appl. Phys. Lett.* 2010. https://doi.org/10.1063/1.3512865.

(76) Dimiev, A.; Kosynkin, D. V.; Sinitskii, A.; Slesarev, A.; Sun, Z.; Tour, J. M. Layer-by-Layer Removal of Graphene for Device Patterning. *Science (80-.).* 2011. https://doi.org/10.1126/science.1199183.

(77) Pirkle, A.; Chan, J.; Venugopal, A.; Hinojos, D.; Magnuson, C. W.; McDonnell, S.; Colombo, L.; Vogel, E. M.; Ruoff, R. S.; Wallace, R. M. The Effect of Chemical Residues on the Physical and Electrical Properties of Chemical Vapor Deposited Graphene Transferred to SiO2. *Appl. Phys. Lett.* 2011. https://doi.org/10.1063/1.3643444.

(78) Zhang, W.; Hu, R.; Li, D.; Huo, M. M.; Ai, X. C.; Zhang, J. P. Primary Dynamics of Exciton and Charge Photogeneration in Solvent Vapor Annealed P3HT/PCBM Films. *J. Phys. Chem. C* 2012. https://doi.org/10.1021/jp211653x.

(79) Tamai, Y.; Ohkita, H.; Benten, H.; Ito, S. Exciton Diffusion in Conjugated Polymers: From Fundamental Understanding to Improvement in Photovoltaic Conversion Efficiency. *J. Phys. Chem. Lett.* 2015. https://doi.org/10.1021/acs.jpclett.5b01147.

(80) Schiros, T.; Nordlund, D.; Pálová, L.; Prezzi, D.; Zhao, L.; Kim, K. S.; Wurstbauer, U.; Gutiérrez, C.; Delongchamp, D.; Jaye, C.; et al. Connecting Dopant Bond Type with Electronic Structure in N-Doped Graphene. *Nano Lett.* 2012. https://doi.org/10.1021/nl301409h.

(81) Madito, M. J.; Bello, A.; Dangbegnon, J. K.; Oliphant, C. J.; Jordaan, W. A.; Masikhwa, T. M.; Momodu, D. Y.; Manyala, N. Raman Analysis of Bilayer Graphene Film Prepared on Commercial Cu(0.5 At% Ni) Foil. *J. Raman Spectrosc.* 2016. https://doi.org/10.1002/jrs.4848.

(82) Park, J. S.; Reina, A.; Saito, R.; Kong, J.; Dresselhaus, G.; Dresselhaus, M. S. G′ Band Raman Spectra of Single, Double and Triple Layer Graphene. *Carbon N. Y.* 2009. https://doi.org/10.1016/j.carbon.2009.01.009.

(83) Tu, Z.; Liu, Z.; Li, Y.; Yang, F.; Zhang, L.; Zhao, Z.; Xu, C.; Wu, S.; Liu, H.; Yang, H.; et al. Controllable Growth of 1-7 Layers of Graphene by Chemical Vapour Deposition. *Carbon N. Y.* 2014. https://doi.org/10.1016/j.carbon.2014.02.061.

(84) Ferrari, A. C.; Basko, D. M. Raman Spectroscopy as a Versatile Tool for Studying the Properties of Graphene. *Nature Nanotechnology*. 2013. https://doi.org/10.1038/nnano.2013.46.

(85) Demirbas, T.; Baykara, M. Z. Nanoscale Tribology of Graphene Grown by Chemical Vapor Deposition and Transferred onto Silicon Oxide Substrates. *J. Mater. Res.* 2016. https://doi.org/10.1557/jmr.2016.11.

(86) Beerbom, M. M.; Lägel, B.; Cascio, A. J.; Doran, B. V.; Schlaf, R. Direct Comparison of Photoemission Spectroscopy and in Situ Kelvin Probe Work Function Measurements on Indium Tin Oxide Films. *J. Electron Spectros. Relat. Phenomena* 2006. https://doi.org/10.1016/j.elspec.2006.02.001.

(87) Wrana, D.; Cieślik, K.; Belza, W.; Rodenbücher, C.; Szot, K.; Krok, F. Kelvin Probe Force Microscopy Work Function Characterization of Transition Metal Oxide Crystals under Ongoing Reduction and Oxidation. *Beilstein J. Nanotechnol.* 2019. https://doi.org/10.3762/bjnano.10.155.

(88) Padovani, F. A.; Stratton, R. Field and Thermionic-Field Emission in Schottky Barriers. *Solid State Electron.* 1966. https://doi.org/10.1016/0038-1101(66)90097-9.

(89) Yim, C.; McEvoy, N.; Duesberg, G. S. Characterization of Graphene-Silicon Schottky Barrier Diodes Using Impedance Spectroscopy. *Appl. Phys. Lett.* 2013. https://doi.org/10.1063/1.4829140.

(90) Güzeldir, B.; Sağlam, M.; Ateş, A.; Türüt, A. Determination of the Some Electronic Parameters of Nanostructure Copper Selenide and Cu/Cu3Se2/n-

GaAs/In Structure. *J. Alloys Compd.* 2015. https://doi.org/10.1016/j.jallcom.2014.11.182.

(91) Kim, D. J.; Kim, G. S.; Park, N. W.; Lee, W. Y.; Sim, Y.; Kim, K. S.; Seong, M. J.; Koh, J. H.; Hong, C. H.; Lee, S. K. Effect of Annealing of Graphene Layer on Electrical Transport and Degradation of Au/Graphene/n-Type Silicon Schottky Diodes. *J. Alloys Compd.* 2014. https://doi.org/10.1016/j.jallcom.2014.05.147.

(92) Liu, J.; Yin, Y.; Yu, L.; Shi, Y.; Liang, D.; Dai, D. Silicon-Graphene Conductive Photodetector with Ultra-High Responsivity. *Sci. Rep.* 2017. https://doi.org/10.1038/srep40904.

(93) Aydin, H.; Kalkan, S. B.; Varlikli, C.; Celebi, C. P3HT-Graphene Bilayer Electrode for Schottky Junction Photodetectors. *Nanotechnology* 2018. https://doi.org/10.1088/1361-6528/aaaaf5.

(94) Liu, F.; Kar, S. Quantum Carrier Reinvestment-Induced Ultrahigh and Broadband Photocurrent Responses in Graphene-Silicon Junctions. *ACS Nano* 2014. https://doi.org/10.1021/nn503484s.

(95) Rashmi; Kapoor, A. K.; Kumar, U.; Balakrishnan, V. R.; Basu, P. K. Degradation Process in Organic Thin Film Devices Fabricated Using P3HT. *Pramana - J. Phys.* 2007. https://doi.org/10.1007/s12043-007-0052-2.

(96) Yu, T.; Wang, F.; Xu, Y.; Ma, L.; Pi, X.; Yang, D. Graphene Coupled with Silicon Quantum Dots for High-Performance Bulk-Silicon-Based Schottky-Junction Photodetectors. *Adv. Mater.* 2016. https://doi.org/10.1002/adma.201506140.

(97) Tongay, S.; Lemaitre, M.; Schumann, T.; Berke, K.; Appleton, B. R.; Gila, B.; Hebard, A. F. Graphene/GaN Schottky Diodes: Stability at Elevated Temperatures. *Appl. Phys. Lett.* 2011. https://doi.org/10.1063/1.3628315.